HAL
open science

The Cosmic Ultraviolet Baryon Survey (CUBS) - I. Overview and the diverse environments of Lyman limit systems at z < 1

Hsiao-Wen Chen, Fakhri S. Zahedy, Erin Boettcher, Thomas M. Cooper, Sean D. Johnson, Gwen C. Rudie, Mandy C. Chen, Gregory L. Walth, Sebastiano Cantalupo, Kathy L. Cooksey, et al.

To cite this version:

Hsiao-Wen Chen, Fakhri S. Zahedy, Erin Boettcher, Thomas M. Cooper, Sean D. Johnson, et al.. The Cosmic Ultraviolet Baryon Survey (CUBS) - I. Overview and the diverse environments of Lyman limit systems at z < 1. Monthly Notices of the Royal Astronomical Society, 2020, 497, pp.498-520. 10.1093/mnras/staa1773 . insu-03748045

HAL Id: insu-03748045

https://insu.hal.science/insu-03748045v1

Submitted on 9 Aug 2022

HAL is a multi-disciplinary open access archive for the deposit and dissemination of scientific research documents, whether they are published or not. The documents may come from teaching and research institutions in France or abroad, or from public or private research centers.

L'archive ouverte pluridisciplinaire **HAL**, est destinée au dépôt et à la diffusion de documents scientifiques de niveau recherche, publiés ou non, émanant des établissements d'enseignement et de recherche français ou étrangers, des laboratoires publics ou privés.

Monthly Notices of the ROYAL ASTRONOMICAL SOCIETY

MNRAS **497,** 498–520 (2020)
Advance Access publication 2020 June 17

doi:10.1093/mnras/staa1773

The Cosmic Ultraviolet Baryon Survey (CUBS) – I. Overview and the diverse environments of Lyman limit systems at $z < 1$

Hsiao-Wen Chen,[1★] Fakhri S. Zahedy,[2] Erin Boettcher,[1] Thomas M. Cooper,[2] Sean D. Johnson,[2,3†] Gwen C. Rudie,[2] Mandy C. Chen,[1] Gregory L. Walth,[2] Sebastiano Cantalupo,[4] Kathy L. Cooksey,[5] Claude-André Faucher-Giguère,[6] Jenny E. Greene,[3] Sebastian Lopez,[7] John S. Mulchaey,[2] Steven V. Penton,[8] Patrick Petitjean,[9] Mary E. Putman,[10] Marc Rafelski,[11,12] Michael Rauch,[2] Joop Schaye,[13] Robert A. Simcoe[14] and Benjamin J. Weiner[15]

[1]*Department of Astronomy & Astrophysics, The University of Chicago, Chicago, IL 60637, USA*
[2]*The Observatories of the Carnegie Institution for Science, 813 Santa Barbara Street, Pasadena, CA 91101, USA*
[3]*Department of Astrophysics, Princeton University, Princeton, NJ 08544, USA*
[4]*Department of Physics, ETH Wolfgang-Pauli-Strasse 27, 8093, CH-8093 Zürich, Switzerland*
[5]*Department of Physics and Astronomy, University of Hawai'i at Hilo, Hilo, HI 96720, USA*
[6]*Department of Physics & Astronomy and Center for Interdisciplinary Exploration and Research in Astrophysics (CIERA), Northwestern University, 1800 Sherman Ave, Evanston, IL 60201, USA*
[7]*Departamento de Astronomía, Universidad de Chile, Casilla 36-D, Santiago, Chile*
[8]*Laboratory For Atmospheric and Space Physics, University of Colorado, Boulder, CO 80303, USA*
[9]*Institut d'Astrophysique de Paris, CNRS-SU, UMR 7095, 98bis bd Arago, Paris F-75014, France*
[10]*Department of Astronomy, Columbia University, New York, NY 10027, USA*
[11]*Space Telescope Science Institute, Baltimore, MD 21218, USA*
[12]*Department of Physics & Astronomy, Johns Hopkins University, Baltimore, MD 21218, USA*
[13]*Leiden Observatory, Leiden University, PO Box 9513, NL-2300 RA Leiden, the Netherlands*
[14]*MIT-Kavli Institute for Astrophysics and Space Research, 77 Massachusetts Ave., Cambridge, MA 02139, USA*
[15]*Steward Observatory, University of Arizona, Tucson, AZ 85721, USA*

Accepted 2020 June 16. Received 2020 June 15; in original form 2020 May 4

ABSTRACT

We present initial results from the Cosmic Ultraviolet Baryon Survey (CUBS). CUBS is designed to map diffuse baryonic structures at redshift $z \lesssim 1$ using absorption-line spectroscopy of 15 UV-bright QSOs with matching deep galaxy survey data. CUBS QSOs are selected based on their NUV brightness to avoid biases against the presence of intervening Lyman limit systems (LLSs) at $z_{\rm abs} < 1$. We report five new LLSs of $\log N({\rm H\,I})/{\rm cm}^{-2} \gtrsim 17.2$ over a total redshift survey path-length of $\Delta z_{\rm LL} = 9.3$, and a number density of $n(z) = 0.43^{+0.26}_{-0.18}$. Considering all absorbers with $\log N({\rm H\,I})/{\rm cm}^{-2} > 16.5$ leads to $n(z) = 1.08^{+0.31}_{-0.25}$ at $z_{\rm abs} < 1$. All LLSs exhibit a multicomponent structure and associated metal transitions from multiple ionization states such as C II, C III, Mg II, Si II, Si III, and O VI absorption. Differential chemical enrichment levels as well as ionization states are directly observed across individual components in three LLSs. We present deep galaxy survey data obtained using the VLT-MUSE integral field spectrograph and the Magellan Telescopes, reaching sensitivities necessary for detecting galaxies fainter than $0.1\,L_*$ at $d \lesssim 300$ physical kpc (pkpc) in all five fields. A diverse range of galaxy properties is seen around these LLSs, from a low-mass dwarf galaxy pair, a co-rotating gaseous halo/disc, a star-forming galaxy, a massive quiescent galaxy, to a galaxy group. The closest galaxies have projected distances ranging from $d = 15$ to 72 pkpc and intrinsic luminosities from $\approx 0.01\,L_*$ to $\approx 3\,L_*$. Our study shows that LLSs originate in a variety of galaxy environments and trace gaseous structures with a broad range of metallicities.

Key words: surveys – galaxies: evolution – galaxies: haloes – quasars: absorption lines.

1 INTRODUCTION

The circumgalactic medium (CGM) and intergalactic medium (IGM) contain fuel for future star formation and a record of past feedback. They are uniquely sensitive to the physics of baryonic flows – one of the principal missing ingredients in our understanding of galaxy evolution (for reviews, see e.g. Somerville & Davé 2015; Naab & Ostriker 2017; Tumlinson, Peeples & Werk 2017). While QSO absorption spectroscopy provides a powerful tool for probing the diffuse gas phase in intergalactic and circumgalactic space, a comprehensive study of the CGM requires matching galaxy survey data. Previous joint galaxy and absorber studies have focused primarily on two

★ E-mail: hchen@oddjob.uchicago.edu
† Carnegie-Princeton Fellow.

© 2020 The Author(s)
Published by Oxford University Press on behalf of the Royal Astronomical Society

Downloaded from https://academic.oup.com/mnras/article/497/1/498/5859973 by CNRS - ISTO user on 09 August 2022

disjoint epochs, $z < 0.4$ (e.g. Chen 2017; Kacprzak 2017; Tumlinson et al. 2017 for recent reviews) and $z \approx 2$ (e.g. Steidel et al. 2010; Rudie et al. 2012; Turner et al. 2014; Rudie et al. 2019). However, as the cosmic star formation rate density (SFRD) declines rapidly from $z \approx 1.5$ to the present day, the CGM remains poorly constrained over a significant fraction of cosmic history (see Burchett et al. 2019 for recent effort in probing the warm-hot CGM through observations of Ne VIII absorption).

Observations of the co-evolution of galaxies with their surrounding gas complements the progress both in wide-field galaxy surveys and in theoretical models of how galaxies form and evolve. In particular, state-of-the-art cosmological simulations, incorporating realistic star formation and feedback recipes, can both match the large-scale statistical properties of galaxies and reproduce the observed small-scale features (e.g. Hopkins et al. 2014; Vogelsberger et al. 2014; Schaye et al. 2015; Wang et al. 2015; Dubois et al. 2016). But these models have fallen short in simultaneously matching the spatial profiles of a wide range of heavy ions (such as Mg^{+}, C^{3+}, O^{5+}) observed in the CGM where the majority of the baryons reside (e.g. Hummels et al. 2013; Liang, Kravtsov & Agertz 2016; Oppenheimer, Crain & Schaye 2016; Nelson et al. 2018; Ji et al. 2019). This mismatch suggests that our understanding of the nature and effects of gas inflows and outflows is still incomplete. Identifying the missing physics that governs the dynamical state of the CGM provides an unparalleled constraint on the manner and mode of feedback in galaxies.

To enable systematic studies of the diffuse CGM and IGM, we are conducting the Cosmic Ultraviolet Baryon Survey (CUBS), which is a large *Hubble Space Telescope* (*HST*) Cycle 25 General Observer Program (GO-CUBS; PID = 15163; PI: Chen). It is designed to map the diffuse baryonic structures at $z \lesssim 1$, using absorption-line spectroscopy of 15 UV bright QSOs with matching deep galaxy survey data. The primary goal of CUBS is to establish a legacy galaxy and absorber sample to enable systematic studies of the co-evolution of galaxies and their surrounding diffuse gas at a time when the SFRD undergoes its most dramatic changes, thereby gaining key insights into how galaxy growth is regulated by accretion and outflows. The CUBS program exploits the synergy between space-based UV spectroscopy and ground-based wide-field surveys, as well as optical Echelle spectroscopy, for advancing a comprehensive understanding of the cosmic evolution of baryonic structures.

Here, we present initial results from the CUBS program, reporting five new Lyman limit systems (LLSs) discovered at $z < 1$ along the CUBS QSO sightlines. In addition, we present the galactic environment of these LLSs uncovered from an ongoing galaxy survey in the CUBS fields, using the Magellan Telescopes and the VLT Multi-Unit Spectroscopic Explorer (MUSE; Bacon et al. 2010). LLSs arise in optically thick gas with opacity $\tau_{912} \gtrsim 1$ to ionizing photons at rest-frame wavelength $\approx$912 Å (or equivalently neutral hydrogen column density $\log N(\mathrm{H\,I})/\mathrm{cm}^{-2} \gtrsim 17.2$). On cosmological scales, the incidence of these optically thick absorbers determines the mean free path of ionizing photons and serves as a key ingredient for computing the photoionization rate in the IGM (e.g. Rudie et al. 2013; Faucher-Giguère 2020). In individual galactic haloes, these absorbers are commonly seen at projected distances $d \lesssim 100$ kpc from known galaxies (e.g. Chen et al. 1998, 2001; Rudie et al. 2012; Thom et al. 2012; Werk et al. 2014; Johnson, Chen & Mulchaey 2015; Prochaska et al. 2017) with a mean covering fraction of $\kappa_{\tau_{912}\geq 1}(d < 100\,\mathrm{kpc}) \gtrsim 70$ per cent (e.g. Chen et al. 2018). The large scatter observed in both gas density and metallicity of the absorbing gas (e.g. Lehner et al. 2019; Zahedy et al. 2019) makes these absorbers a promising signpost of either infalling clouds (e.g. Maller & Bullock 2004; Faucher-Giguère & Kereš 2011; Fumagalli et al. 2011; van de Voort et al. 2012; Afruni, Fraternali & Pezzulli 2019) or outflows (e.g. Faucher-Giguère et al. 2015, 2016) in galactic haloes, or a combination thereof (e.g. Hafen et al. 2017). We examine these different scenarios based on the galaxy environment revealed in the accompanying galaxy survey data.

The paper is organized as follows. In Section 2, we describe the design of the CUBS program and related spectroscopic observations. We describe the search and identification of LLSs along the CUBS QSO sightlines in Section 3, and their galactic environments in Section 4. In Section 5, we discuss the implications of our findings. Throughout the paper, we adopt a standard Λ cosmology, $\Omega_{\mathrm{M}} = 0.3$ and $\Omega_{\Lambda} = 0.7$ with a Hubble constant $H_0 = 70\,\mathrm{km\,s^{-1}\,Mpc^{-1}}$.

2 THE CUBS PROGRAM

The CUBS program is designed to map the dominant cosmic baryon reservoirs in intergalactic and circumgalactic space at intermediate redshifts using QSO absorption spectroscopy, bridging the gap between existing efforts at $z < 0.4$ and at $z \approx 2$. It utilizes the high UV throughput and medium spectral resolution offered by the Cosmic Origins Spectrograph (COS; Green et al. 2012) on board *HST* for probing the physical conditions and chemical content of diffuse gas based on observations of a suite of absorption transitions from different ions. Specifically, COS with the G130M and G160M gratings provides spectral coverage over $\lambda = 1100$–1800 Å for a wide range of ionic transitions at $z < 1$. These include the hydrogen Lyman-series transitions and heavy elements such as carbon, nitrogen, oxygen, silicon, sulfur, etc. in several ionization states (examples are presented in Boettcher et al., in preparation; Cooper et al., in preparation; Johnson et al., in preparation; Zahedy et al., in preparation). An added bonus of targeting the redshift range at $z > 0.4$ is the ability to precisely measure the neutral hydrogen column density, $N(\mathrm{H\,I})$, using the higher order Lyman series absorption transitions (e.g. Rudie et al. 2013; Chen et al. 2018; Zahedy et al. 2019).

In addition, a critical component of the CUBS program is a comprehensive deep galaxy survey in the fields around these 15 QSOs. The locations and properties of galaxies, together with the absorption properties of associated haloes from the COS spectra, provide direct constraints for feeding and feedback in galactic haloes. Our galaxy survey is carried out both in space using the Wide Field Camera 3 (WFC3) and the IR channel in parallel slitless grism mode, and on the ground using the VLT and Magellan telescopes. The slitless grism spectroscopy utilizes the G102 and G141 grisms to target nebular lines such as [O III], H β, and H α at $z \lesssim 1$ from galaxies as faint as $AB(H) \approx 23-24$ mag. While the field will be offset by 3–4 Mpc from the QSO, it complements the ground-based galaxy survey for mapping the large-scale structures in the QSO fields.

The ground-based galaxy survey consists of three components: (1) a *shallow and wide* component using the IMACS multi-object imaging spectrograph (Dressler et al. 2006) on the Magellan Baade telescope to target L_* galaxies at $z_{\mathrm{gal}} \lesssim 0.8$ and angular distances at $\theta \lesssim 10$ arcmin (corresponding to $d < 3$–5 physical Mpc) from the QSO sightline, (2) a *deep and narrow* component using the Low Dispersion Survey Spectrograph 3 on the Magellan Clay telescope to target all galaxies as faint as $0.1\,L_*$ up to $z \approx 1$ (and fainter at lower redshifts) at $\lesssim 3$ arcmin in angular radius (corresponding to $d < 300$–500 physical kpc; pkpc) from the QSO sightline, and (3) an *ultradeep* component using MUSE on the VLT UT4 to target galaxies as faint as $\approx 0.01\,L_*$ at $z \approx 1$ at $\lesssim 30$ arcsec in angular radius (corresponding to $d < 250$ physical kpc) from the QSO sightline. The *shallow and wide* component will enable large-scale ($\approx$1–10 Mpc)

Downloaded from https://academic.oup.com/mnras/article/497/1/498/5859973 by CNRS - ISTO user on 09 August 2022

cross-correlation studies between gas and galaxies. The *ultradeep* and *deep and narrow* components enable detailed studies of gas flows and the chemical enrichment in the CGM at projected distances $d \lesssim 300$ pkpc from galaxies with mass as low as $M_{\rm star} \sim 10^9\,{\rm M}_\odot$ at $z \lesssim 1$. The primary scientific objectives are (1) to measure the cosmic mass density evolution of heavy ions; (2) to determine the metallicity and ionization state of the diffuse CGM and IGM; (3) to constrain the origin and evolution of the chemically enriched CGM in haloes of different masses and star formation histories; and (4) to investigate the environmental effects in distributing heavy elements beyond galaxy haloes. Here, we describe the program design and associated spectroscopic observations.

2.1 Program design

To facilitate a systematic and unbiased study of the CGM/IGM at $z \approx 0.4$–1, the CUBS QSOs are selected to be at $z_{\rm QSO} \gtrsim 0.8$ and bright in the *GALEX* near-UV bandpass (NUV; 1770–2730 Å). The QSOs are selected from existing surveys with available spectra for redshift confirmations, including the Hamburg/ESO survey (Wisotzki et al. 2000), the Sloan Digital Sky Survey (SDSS; York et al. 2000; Eisenstein et al. 2011), the Ultraviolet-bright Quasar Survey (UVQS; Monroe et al. 2016), and our own spectroscopic observations for confirmations. Redshift uncertainties are typically $dz/(1+z) \approx 0.002$ for the UVQS and significantly better for SDSS (e.g. Hewett & Wild 2010). By targeting QSOs at $z_{\rm QSO} = 0.8$–1.3, we optimize the survey efficiency and maximize the survey path-length offered by the spectral coverage of COS for each QSO sightline.

The NUV magnitude-limited QSO selection criterion is motivated by the expectation that the presence of an LLS or a pLLS at $z \lesssim 0.9$ attenuates the background QSO light in the far-UV channel (FUV; 1350–1780 Å; see the top panel of Fig. 1). Consequently, targeting known FUV-bright QSOs at $z_{\rm QSO} \gtrsim 0.8$ would impose a bias against sightlines intercepting an LLS or partial LLS at lower redshifts. Finally, we select the QSOs from regions covered by the Dark Energy Survey[1] (DES; e.g. Drlica-Wagner et al. 2018) on the ground. The available DES g, r, i, z, Y images are supplemented with deeper g, r, and near-infrared H-band images from the Magellan Telescopes to enable systematic studies of galaxy environments of individual absorbers.

To obtain a representative map of the dominant cosmic baryon reservoir at $z = 0.4$–1, the targeted sample size is defined such that (1) a statistically representative sample of ≈100 of 0.1 L_*–L_* galaxies at $z > 0.4$ can be established for a comprehensive study of the CGM and (2) a large redshift path-length is reached for IGM metal-absorption-line surveys. Based on the best-fitting luminosity functions for red and blue galaxies from Cool et al. (2012), we estimate that 15 QSO fields are needed for establishing a sample of ≈75 blue, star-forming and ≈30 red, evolved galaxies over a wide range of luminosity at redshifts between $z_{\rm gal} \approx 0.4$ and $z_{\rm gal} \approx 0.8$ and projected distances $d < 300$ pkpc from the QSO sightlines. In addition, a complete galaxy survey carried out in these CUBS fields will also double the number of $z < 0.4$ galaxies with known CGM constraints. Furthermore, combining 15 new CUBS QSOs and available archival sightlines is expected to lead to the largest redshift survey path-length of $\Delta z \approx 8$ (13) for high-ionization species probed by the O VI λλ 1031, 1037 and Ne VIII λλ 770, 780 doublets at $z > 0.4$. These represent new samples of O VI and Ne VIII absorbers that are statistically significant in size for robust measurements of the frequency distribution function and the cosmic mass density of these highly ionized species. Because the absorber samples are drawn from random sightlines, they probe diverse gaseous environments (i.e. from interstellar to circumgalactic and intergalactic space).

[1] https://www.darkenergysurvey.org/

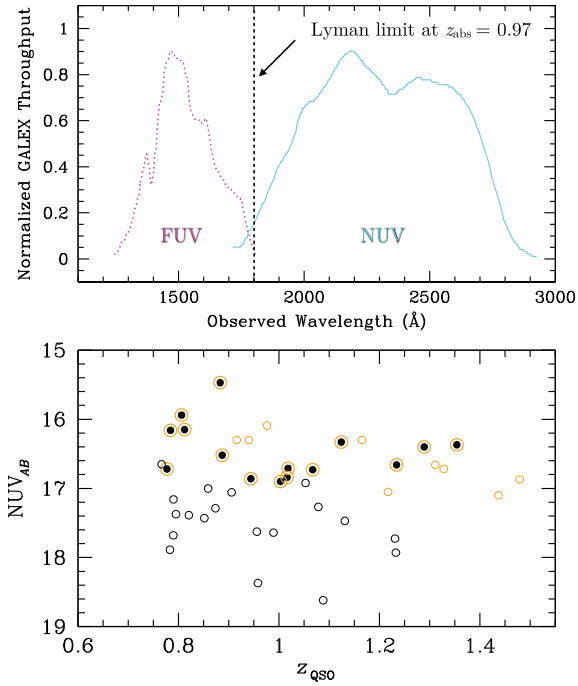

Figure 1. *Top*: Normalized throughput functions for the *GALEX* FUV (dotted magenta curve) and NUV (solid cyan curve) bandpasses. LLSs at $z_{\rm abs} \lesssim 0.97$ attenuate the observed FUV flux in the background QSO. A FUV-bright QSO sample would therefore be biased against these low-redshift LLSs. Therefore, CUBS QSOs are selected based on their NUV brightness. *Bottom*: NUV magnitude versus redshift distribution of $z_{\rm QSO} > 0.7$ QSOs with UV spectra available in the *HST* archive. Those with available high-quality COS UV spectra of S/N $\gtrsim 15$ resel^{-1} are highlighted in orange circles, and those obtained as part of the CUBS program are shown in solid points.

The QSO fields are selected blindly without prior knowledge of the line-of-sight galactic environment. A lesson learned from previous CGM experiments is that preferentially selecting QSO fields with a larger number of known photometrically selected galaxies does not necessarily help increase the galaxy sample size for a fixed number of QSO fields but likely biases the galaxy sample towards galaxy groups (see e.g. Werk et al. 2012; Qu & Bregman 2018). The inclusion of galaxy groups not only skews the galaxy sample towards more massive haloes but also introduces ambiguities in interpreting the physical connections between the absorber and multiple group members. The QSOs in the CUBS program are presented in Table 1. Fig. 1 (bottom panel) presents the NUV magnitude versus redshift distribution of known UV bright QSOs at $z_{\rm QSO} > 0.7$. The CUBS QSOs are highlighted in solid points, showing a three-fold increase in the number of high-quality UV absorption spectra at $z_{\rm QSO} > 0.7$.

2.2 COS UV spectroscopy

Medium-resolution, high signal-to-noise ratio (S/N) FUV spectra of 15 new NUV bright QSOs were obtained under the CUBS program (PID = 15163; PI: Chen) using COS on board the *HST*. COS with the G130M and G160M gratings and a combination of multiple central wavelength settings (see Table 2) offers a contiguous spectral coverage of λ = 1100–1800 Å, with a spectral

Downloaded from https://academic.oup.com/mnras/article/497/1/498/5859973 by CNRS - ISTO user on 09 August 2022

Table 1. Summary of the CUBS QSO sample.

QSO	RA(J2000)	Dec.(J2000)	z_{QSO}	FUV (mag)	NUV (mag)	Ref.
J0028−3305	00:28:30.405	−33:05:49.25	0.887	17.33	16.52	(1)
J0110−1648	01:10:35.511	−16:48:27.70	0.777	17.31	16.72	(2)
J0111−0316	01:11:39.171	−03:16:10.89	1.234	18.47	16.66	(3)
J0114−4129	01:14:22.123	−41:29:47.29	1.018	18.33	16.71	(4)
J0119−2010	01:19:56.091	−20:10:22.73	0.812	16.86	16.15	(5)
J0154−0712	01:54:54.682	−07:12:22.17	1.289	17.07	16.40	(3)
J0248−4048	02:48:06.286	−40:48:33.66	0.883	16.11	15.47	(4)
J0333−4102	03:33:07.076	−41:02:01.15	1.124	17.60	16.33	(4)
J0357−4812	03:57:21.918	−48:12:15.16	1.016	17.76	16.84	(6)
J0420−5650	04:20:53.907	−56:50:43.96	0.944	17.61	16.86	(4)
J0454−6116	04:54:15.952	−61:16:26.56	0.784	16.89	16.16	(3)
J2135−5316	21:35:53.202	−53:16:55.82	0.806	17.13	15.94	(3)
J2308−5258	23:08:37.796	−52:58:48.94	1.067	17.97	16.73	(4)
J2339−5523	23:39:13.218	−55:23:50.84	1.354	17.91	16.37	(4)
J2245−4931	22:45:00.207	−49:31:48.46	1.003	18.10	16.90	(3)

Note. References: (1) Lamontagne et al. (2000), (2) Perlman et al. (1998), (3) Monroe et al. (2016), (4) Wisotzki et al. (2000), (5) Jones et al. (2009), (6) Savage et al. (1976).

Table 2. Journal of CUBS *HST* COS observations.

QSO	z_{QSO}	t_{exp} (s) G130M[a]	G160M[b]	$\langle S/N \rangle_{resel}$
J0028−3305	0.887	13253	17589	23
J0110−1648	0.777	15320	19802	31
J0111−0316	1.234	15149	19711	20
J0114−4129	1.018	15320	19798	12
J0119−2010	0.812	7049	13437	24
J0154−0712	1.289	9716	14843	28
J0248−4048	0.883	4516	5538	20
J0333−4102	1.124	12534	14849	24
J0357−4812	1.016	32664	24630	27
J0420−5650	0.944	17797	20570	22
J0454−6116	0.784	8330	13503	22
J2135−5316	0.806	7098	9738	18
J2245−4931	1.003	9395	19321	14
J2308−5258	1.067	20618	22118	23
J2339−5523	1.354	9388	14987	22

[a]Two central wavelength settings, C1291 and C1223, were used for a contiguous spectral coverage.
[b]Four central wavelength settings, C1577, C1589, C1611, and C1623 were used.

resolution of full width at half-maximum $\delta v_{FWHM} \approx 20$ km s^{-1} for observing a wide range of ionic transitions at $z < 1$. These include the hydrogen Lyman-series transitions from Ly α and Ly β onward to the Lyman-limit transition, and heavy-element transitions such as O III λ 702, Ne VIII $\lambda\lambda$ 770, 780, O IV λ 787, O II λ 834, C II $\lambda\lambda$ 903a, b, C III λ 977, O I λ 988, O VI $\lambda\lambda$ 1031, 1037, etc. The full coverage of the H I Lyman series enables precise and accurate measurements of the neutral hydrogen column density N(H I). The relative abundances between different ions enable accurate estimates of the ionization state and metallicity of the gas.

All COS target acquisitions (TA) were performed using S/N > 50 ACQ/IMAGEs. Analysis of the primary and confirmation images reveal that all targets were centred to better than 0.015 arcsec (0.016 arcsec) along the dispersion (cross-dispersion) direction. For G130M and G160M spectra, the dispersion velocity offsets due to TA are less than 1.5 km s^{-1}. A summary of the COS observations is presented in Table 2, which lists for each QSO, the name and redshift of the QSO, the total exposure time per grating in seconds, and the mean S/N per resolution element, $\langle S/N \rangle_{resel}$ in the final combined spectrum.

Raw data from COS were reduced following standard pipeline procedures using CALCOS (v3.3.4 or v3.3.5). In addition, individual one-dimensional spectra were further processed and combined using custom software to ensure the accuracy of wavelength calibration and to optimize the S/N in the final combined spectra. A detailed description of the software can be found in Chen et al. (2018). In summary, *relative* wavelength offsets between individual spectra were first determined using a low-order polynomial that best describes the offsets between common absorption lines found in different exposures. These wavelength-corrected spectra were then coadded to form a final combined spectrum using individual exposure times as weights. The final *absolute* wavelength calibration was guided by either the line-of-sight velocity offset of the Milky Way Ca II H&K lines or the redshift of a strong intervening Mg II absorber detected in the ground-based MIKE optical Echelle spectrum of the QSO (see Section 2.3 below), which sets the wavelengths for the associated FUV transitions in the COS spectra. A mean wavelength zero-point offset was then determined by registering the associated low-ionization lines observed in the COS spectra to the expected wavelength in vacuum. The final wavelength solution generated from our custom software was found to be accurate to within ± 5 km s^{-1}, based on comparisons of the velocity centroids between low-ionization lines observed in COS spectra and those of Mg II $\lambda\lambda$ 2796, 2803 lines observed in higher resolution ground-based Echelle spectra ($\delta v_{FWHM} \approx 8$–10 km s^{-1}). Finally, each combined spectrum was continuum-normalized using a low-order polynomial fit to spectral regions free of strong absorption features. The final continuum-normalized spectra have a median $\langle S/N \rangle_{resel} \approx 12$–31 (see Table 2). The large variation in the S/N of the final combined spectra is largely due to QSO variability. For example, comparing S/N in the final COS spectra and known *GALEX* magnitudes of the QSOs, we estimate that J0110−1648 had brightened by a factor of ≈1.4, while J0114−4129 had faded by a factor of 2 since the *GALEX* observations. Large QSO variability was also directly observed in the COS spectra of J2308−5258 obtained several months apart.

2.3 Optical Echelle spectroscopy

We complement the FUV spectra from COS with optical Echelle spectra of the QSOs, obtained using MIKE (Bernstein et al. 2003)

Downloaded from https://academic.oup.com/mnras/article/497/1/498/5859973 by CNRS - ISTO user on 09 August 2022

Table 3. Journal of CUBS Magellan MIKE observations.

QSO	z_{QSO}	V (mag)	t_{exp} (s)	FWHM (km s^{-1})	$\langle$S/N$\rangle_{resel}$ 3500 Å	4500 Å
J0028−3305	0.887	16.4	2100	8	6	35
J0110−1648	0.777	16.0	1800	8	12	38
J0111−0316	1.234	15.5	1800	8	18	55
J0114−4129	1.018	16.7	3600	8	10	42
J0119−2010	0.812	15.8	1800	8	16	55
J0154−0712	1.289	15.8	1500	8	14	42
J0248−4048	0.883	15.1	900	8	13	48
J0333−4102	1.124	15.8	2700	10	20	65
J0357−4812	1.016	16.0	5400	10	12	41
J0420−5650	0.944	16.1	3000	10	8	30
J0454−6116	0.784	15.8	1800	10	17	58
J2135−5316	0.806	15.8	3200	8	14	64
J2245−4931	1.003	16.5	3600	8	6	35
J2308−5258	1.067	16.2	5800	8	11	52
J2339−5523	1.354	15.5	2700	8	15	78

on the Magellan Clay telescope. MIKE delivers an unbinned pixel resolution of 0.12 arcsec (0.13 arcsec) along the spatial direction and ≈0.02 (0.05) Å along the spectral direction in the blue (red) arm, covering a wavelength range of λ = 3200–5000 (4900–9200) Å. It provides extended spectral coverage for additional ionic transitions through observations of the Fe II absorption series, the Mg II $\lambda\lambda$ 2796, 2803 doublet features, Mg I λ 2852, and Ca II $\lambda\lambda$ 3934, 3969 absorption, and enables accurate relative abundances studies (e.g. Zahedy et al. 2016, 2017).

The majority of the optical Echelle spectra of the CUBS QSOs were obtained between 2017 September and 2018 March, with additional observations taken in 2019 February and 2019 October. These UV-bright QSOs are also bright in the optical window, with V-band magnitude ranging from V = 15.1 mag to V = 16.5 mag. The Echelle spectroscopy of CUBS QSOs was carried out as a filler program within other regular programs. As a result, two readout settings, 2 × 2 versus 3 × 3 binning, were adopted for the QSO sample, leading to a spectral resolution of $\delta\, v_{\rm FWHM} \approx 8$, and 10 km s^{-1}, respectively. The Echelle spectra were processed and extracted using custom software described in Chen et al. (2014) and in Zahedy et al. (2016). Wavelength calibrations were performed using a ThAr frame obtained immediately after each science exposure and subsequently corrected to a vacuum and heliocentric wavelength scale. Relative flux calibrations were performed using a sensitivity function determined from a spectrophotometric standard star observed on the same night as the CUBS QSOs. Individual flux-calibrated Echelle orders from different exposures were then coadded and combined to form a single final spectrum. Finally, the combined spectrum was continuum-normalized using a low-order polynomial fit to the spectral regions free of strong absorption features.

A summary of available optical Echelle spectra is presented in Table 3, which lists for each QSO the V-band magnitude, the total accumulated exposure time, spectral resolution, and the mean S/N per resolution element at λ = 3500 and 4500 Å. The mean S/N$_{\rm resel}$ of the final combined spectra ranges between 6 and 20 at λ = 3500 Å and between 30 and ≈80 at λ = 4500 Å. These Echelle spectra offer a factor of two larger resolving power for metal lines than the FUV spectra from COS. They serve as an important guide for analysing the COS spectra.

Table 4. Journal of completed MUSE-LLS observations.

QSO	t_{exp} (s)	FWHM (arcsec)	$AB(r)^a$ (mag)	SB(7000 Å)^b (erg s^{-1} cm^{-2} Å^{-1} arcsec^{-2})
J0248−4048^c	7650	0.7	27.0	9.8×10^{-20}
J0357−4812	9390	0.6	27.4	7.5×10^{-20}
J2135−5316	6840	0.6	26.9	1.3×10^{-19}

^{a}5σ limiting magnitude in the pseudo r band integrated from 6000 to 7000 Å.
^{b}1σ limiting surface brightness at 7000 Å arcsec^{-2} aperture.
^{c}One of the OBs for J0248−4048 was obtained through clouds. While the exposures through clouds do not reach the same depth as those obtained under clear skies, including all exposures yields the deepest combined data cube for this field.

2.4 MUSE observations

The *ultradeep* galaxy survey component described at the beginning of Section 2 is being carried out using the MUSE (Bacon et al. 2010) on the VLT UT4 in service mode under program ID, 0104.A-0147 (PI: Chen). MUSE observes a field of 1 armin × 1 arcmin with a plate scale of 0.2 arcsec and 1.25 Å pixel^{-1}, covering a spectral range from 4800 to 9200 Å with a spectral resolution of $\delta\, v_{\rm FWHM} \approx 120$ km s^{-1} at 7000 Å. The combined spatial and spectral resolving power of MUSE provides high sensitivity and high efficiency for surveys of distant faint galaxies and line-emitting nebulae, and is uniquely suitable for uncovering faint emission close to QSO sightlines (e.g. Schroetter et al. 2016; Bielby et al. 2017; Johnson et al. 2018; Chen et al. 2019a, b; Péroux et al. 2019). For the CUBS QSO fields, the combination of *HST* COS absorption spectroscopy and MUSE integral-field spectroscopy provides a powerful tool for studying the complex interplay between gas and galaxies at $z \lesssim 1$.

The CUBS-MUSE program aims to uncover galaxies as faint as ≈0.01 L_* at $z \lesssim 1$ near the QSO sightlines. The observations are carried out in wide-field mode (WFM) with adaptive optics assistance. While the use of lasers for wavefront corrections imposes a gap in the spectral coverage from 5800 to 5965 Å, it ensures a uniform mean image quality of FWHM < 0.8 arcsec across all fields. For each CUBS QSO field, the MUSE observations are carried out in a series of two to three observing blocks (OBs) with individual OBs consisting of three exposures of 850–1130 s each. To optimize cosmic ray rejection and minimize a fixed residual flat-field pattern at the edges of individual slicers, a small dither of ≈2–4 arcsec and a relative field rotation of 90° are applied to every successive exposure. While the program is ongoing, here we present results from three completed CUBS QSO fields, all with an LLS found in the foreground (see Section 3 below). The QSO fields and the total accumulated exposure time with MUSE are presented in the first two columns of Table 4.

All MUSE data cubes are reduced using a combination of the standard ESO MUSE pipeline (Weilbacher et al. 2014) and CUBEXTRACTOR, a custom package developed by S. Cantalupo (see Cantalupo et al. 2019 for a detailed description). For each OB, both raw science exposures and the associated raw calibration files, including bias, flats, comparison arc files, and spectrophotometric standard, are retrieved from the ESO science archive. The ESO MUSE pipeline first generates a master bias and a master flat, processes the arcs for wavelength calibration and for measuring the instrument line spread function, and twilight flats for illumination corrections. Then it applies these calibrations to the standard star and science frames to produce a response function, telluric corrections, and a sky continuum using the 20 per cent darkest pixels in the

Downloaded from https://academic.oup.com/mnras/article/497/1/498/5859973 by CNRS - ISTO user on 09 August 2022

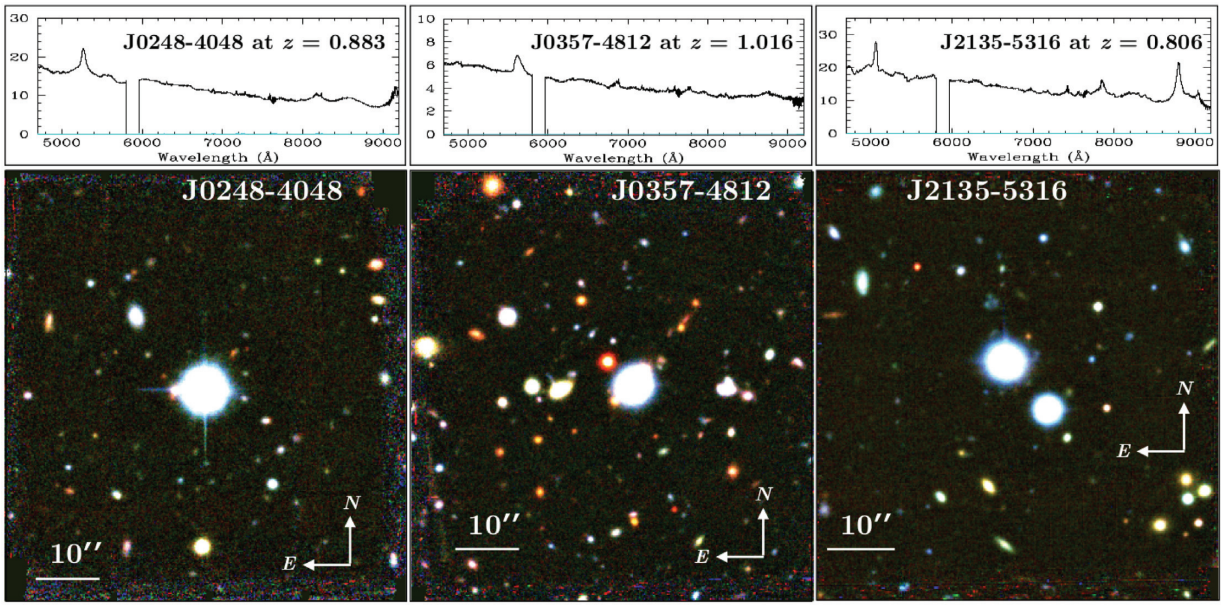

Figure 2. MUSE observations of three CUBS QSO fields. Optical spectra of the QSOs extracted from the combined MUSE data cube are presented at the *top*, showing the spectral coverage of MUSE. The spectral gap at 5800–5965 Å in the top panels is due to the sodium filter, which was applied to block the scattered light from the laser beams for wavefront corrections. Continuum images of the QSO fields are presented at the *bottom*. The colour images are produced from integrating the MUSE cube over wavelength ranges of 4800–5800 Å (pseudo *g* band), 6000–7000 Å (pseudo *r* band), and 7500–8500 Å (pseudo *i* band). For each field, north is up and east is to the left. The QSO is at the centre, and the horizontal bar in the lower-left corner marks 10 arcsec on the sky.

field of view. Finally, the pipeline produces a sky-subtracted 3D data cube for each raw science exposure, along with associated pixel tables storing all calibration parameters, and a whitelight image for object identifications. Individual data cubes are then registered using common objects identified in the corresponding whitelight image to form a final combined cube for each OB.

The final product from the standard ESO pipeline exhibits apparent residual patterns in the sky background due to imperfect illumination correction and sky subtraction (see fig. 1 of Lofthouse et al. 2020 for an example). The residuals are most severe near/at bright sky lines, making robust identifications of faint features challenging. In particular, MUSE consists of 24 integral field units (IFUs) and each IFU consists of four stacks of 12 slices. Any temporal and wavelength-dependent changes in the illumination pattern and instrument line spread function result in large background residuals in the final data cube. To improve upon the standard pipeline reduction, the CUBEXTRACTOR package first adopts the pipeline produced data cube with sky subtraction turned off to define a reference grid for the post-processing steps and resamples the pixel tables on to the reference grid. Then "CubeFix" works in the reconstructed data cube space and empirically determines a wavelength-dependent illumination pattern per image slice using the sky background observed in each science frame. Next, 'CubeSharp' performs a flux-conserving (across the field of view) sky subtraction routine using an empirical line spread function constructed from the skylines recorded in the science frame. These steps are performed twice using an updated object catalogue for masking continuum sources in the second iteration of sky removal. Finally, individually corrected data cubes from all OBs are combined to form a final data cube. Because the MUSE wavelength solution is calibrated in air and QSO absorption spectra are calibrated to vacuum, the product of CUBEXTRACTOR is further resampled to vacuum wavelength to facilitate an accurate redshift comparison between galaxies identified in MUSE and absorbers identified in the COS spectra.

The QSO spectra and RGB images constructed using pseudo *g*-, *r*-, and *i*-band images integrated over wavelength windows of 4800–5800, 6000–7000, and 7500–8500 Å, respectively, from the final MUSE data cubes of the three CUBS QSO fields are presented in Fig. 2. The image quality in the final combined cubes ranges between FWHM $\approx$ 0.6 and 0.7 arcsec at 7000 Å. The image quality is slightly worse at shorter wavelengths, ranging from $\approx$0.7 to 0.8 arcsec at 5000 Å, and better at longer wavelengths, ranging from $\approx$0.56 to 0.6 arcsec at 9000 Å. The 5σ limiting magnitude in the pseudo *r* band ranges between $r = 27.0$ and 27.4 mag over 1 arcsec diameter aperture and the 1σ limiting surface brightness reaches (0.8–1.3) $\times 10^{-19}$ erg s^{-1} cm^{-2} Å^{-1} arcsec^{-2} at 7000 Å arcsec^{-2} aperture (see Table 4).

3 SURVEY OF LYMAN LIMIT ABSORBERS AT $z < 1$

The CUBS QSOs are selected based on the QSO emission redshift with $z_{\rm QSO} \gtrsim 0.8$ and the NUV brightness with NUV $\lesssim$ 16.9 (Fig. 1), with no prior knowledge of the line-of-sight absorption properties or galactic environment. Therefore, the CUBS QSO sample provides a uniform sample (cf. archival samples from Ribaudo et al. 2011 or Shull et al. 2017) for studying the incidence of optically thick gas at $z \lesssim 1$ as well as the connection between LLS and galaxy properties. The COS spectra described in Section 2.2 are of sufficiently high quality with S/N$_{\rm resel} > 12$ to enable a robust identification of both the Lyman discontinuity at $\approx$912 Å and the Lyman series lines at longer wavelengths. Here, we describe the procedures we use to identify these absorbers and to measure N(H I).

3.1 The search for Lyman continuum breaks

The search for LLS in the CUBS QSO sample is carried out using the following steps. For each QSO sightline, a minimum redshift $z_{\rm min}$

Downloaded from https://academic.oup.com/mnras/article/497/1/498/5859973 by CNRS - ISTO user on 09 August 2022

Table 5. Summary of new (p)LLSs in the CUBS fields.

Field (1)	$z_{\rm min}$ (2)	$z_{\rm max}$ (3)	$\Delta z_{\rm LL}$ (4)	$z_{\rm abs}$ (5)	τ_{912} (6)
J0028−3305	0.21	0.87	0.66	–	–
J0110−1648	0.20	0.76	0.56	0.4723[a]	0.18 ± 0.01
				0.5413[a]	0.21 ± 0.01
J0111−0316	0.57	0.94	0.37	0.5762[b]	>6.61
J0114−4129	0.23	0.94	0.71	0.3677	0.16 ± 0.02
				0.9001	0.41 ± 0.03
J0119−2010	0.21	0.79	0.58	–	–
J0154−0712	0.20	0.94	0.74	0.3743	0.24 ± 0.01
J0248−4048	0.24	0.86	0.62	0.3640	2.48 ± 0.01
J0333−4102	0.20	0.94	0.74	0.9372	0.61 ± 0.02
J0357−4812	0.21	0.94	0.73	0.4353	0.99 ± 0.01
J0420−5650	0.21	0.92	0.71	–	–
J0454−6116	0.21	0.76	0.55	–	–
J2135−5316	0.62	0.79	0.17	0.6226	>6.27
J2245−4931	0.22	0.94	0.72	–	–
J2308−5258	0.22	0.94	0.72	0.2603	0.58 ± 0.02
				0.5427	2.53 ± 0.01
J2339−5523	0.21	0.94	0.73	–	–

[a]See Cooper et al. (in preparation).
[b]See Boettcher et al. (in preparation).

for the LLS search is defined by the minimum wavelength where $S/N_{\rm resel} > 3$, while the maximum survey redshift $z_{\rm max}$ is defined by either the maximum wavelength of the COS spectrum or the emission redshift of the QSO, excluding the velocity window of $|\Delta v| = 3000$ km s^{-1} from $z_{\rm QSO}$ to avoid the QSO proximity zone where the ionizing radiation intensity is expected to be enhanced due to the background QSO (e.g. Pascarelle et al. 2001; Wild et al. 2008). Table 5 summarizes $z_{\rm min}$ and $z_{\rm max}$ for each CUBS QSO, along with the redshift survey path-length $\Delta z_{\rm LL}$, in columns (2)–(4). Together, the 15 CUBS QSOs provide a total redshift survey path-length of $\Delta z_{\rm LL} = 9.3$ for new LLSs.

Each Lyman limit absorber is then identified based on an apparent flux discontinuity in the QSO spectrum and verified based on the presence of associated Lyman series lines. A total of 12 such absorbers are found along nine of the 15 QSO sightlines, with the remaining six sightlines displaying no evident continuum breaks in the COS spectral window.[2] A mean opacity, τ_{912}, is determined based on the observed flux decrement at 911.76 Å relative to the expected continuum flux from extrapolating a linear model that best describes the continuum at rest-frame 920–923 Å at the redshift of the absorber, $z_{\rm abs}$. The error in τ_{912} is estimated including uncertainties in both the continuum model and the measurement uncertainties in the mean flux observed at rest-frame 911.76 Å. The results, including $z_{\rm abs}$, are presented in columns (5)–(6). Of the 12 absorbers identified based on an apparent Lyman discontinuity, five are LLSs with $\tau_{912} \gtrsim 1$ at $z_{\rm abs} = 0.36$–0.62 and five are partial LLSs (pLLSs) with τ_{912} from 0.2 to $\lesssim 1$ at $z_{\rm abs} = 0.26$–0.94. Fig. 3 presents the full Lyman series spectra of the five new LLSs from this search in descending order of N(H I).

3.2 Measurements of N(H I) and $b_{\rm H\,I}$

In addition to the prominent Lyman discontinuity, Fig. 3 also shows that each of these new LLSs is resolved into multiple components of varying absorption strength. The resolved component structure is clearly displayed in the velocity profiles of both H I and the associated metal lines presented in Fig. 4. In particular, higher resolution ($\delta\, v_{\rm FWHM} \approx 8$ km s^{-1}) ground-based optical Echelle spectra show that the associated Mg II doublets of these LLSs are resolved into between two and six well-defined components.

To obtain accurate measurements of N(H I) for individual components, we perform a Voigt profile analysis that takes into account the full Lyman series lines and the observed flux discontinuity at the Lyman limit (see also Chen et al. 2018; Zahedy et al. 2019). We first generate a model absorption spectrum based on the minimum number of discrete components required to explain the observed absorption profiles. This process is guided by the component structure of the associated Mg II doublet for each LLS. Each component is characterized by three parameters: $N(H\,{\rm I})$, $b_{\rm H\,I}$, and the velocity centroid dv_c relative to the redshift of the strongest H I absorbing component $z_{\rm abs}$. The model Lyman series spectrum is then convolved with the COS line spread function (LSF) appropriate for Lifetime Position 4, at which the spectra were recorded. Next, we perform a χ^2 minimization routine to determine the best-fitting model parameters by comparing the LSF-convolved model spectrum with observations. For H I components with associated Mg II, dv_c is fixed at the location determined from the centroid of the Mg II component. For H I components without detected Mg II, dv_c is allowed to vary during the χ^2 minimization routine.[3]

To estimate the uncertainties associated with the best-fitting parameters, we perform a Markov chain Monte Carlo (MCMC) analysis using the EMCEE package (Foreman-Mackey et al. 2013). The MCMC analysis consists of 300 steps with an ensemble of 250 walkers, initialized over a small region in the parameter space around the minimum χ^2 value. The first 100 steps of each walker are discarded when constructing a probability distribution function for each best-fitting model parameter from combining results from all 250 walkers. The MCMC approach enables a robust evaluation of correlated errors between blended components over a reasonable amount of computing time. The results of the Voigt profile analysis are summarized in Table 6, where for each LLS the best-fitting redshift of the strongest H I component $z_{\rm abs}$ and the total N(H I) summed over all components are listed, along with the best-fitting velocity centroid dv_c relative to $z_{\rm abs}$, N_c(H I), b_c(H I) and associated 1σ uncertainties for individual components.

The best-fitting Voigt profiles of individual H I components are shown in Fig. 3 for the Lyman series from Ly γ to the Lyman break, with the red spectrum representing the integrated profile over all components. The best-fitting models are also displayed in the top two rows of Fig. 4 for Ly β and Ly γ to contrast the velocity structures displayed in the associated ionic transitions. In all five LLSs, a dominant component, containing between 75 per cent and 98 per cent of the total H I column density, is needed to explain the high-order Lyman series profiles, while additional satellite components are needed to explain the widths and asymmetric profiles observed in lower order Lyman lines such as Ly α through Ly δ. With the exception of the LLS at $z_{\rm abs} = 0.4353$ towards J0357−4812,

[2]We note the presence of a likely LLS at $z_{\rm abs} \approx 1$ towards J2339−5523 based on the observed spectral slope of the QSO and a suite of absorption transitions in the COS data. This system will be presented in Johnson et al. (in preparation).

[3]One exception is the absorber at $z_{\rm abs} = 0.5762$ towards J0111−0316, which turns out to be an H_2-bearing DLA, for which all available Lyman series lines are highly saturated, preventing us from resolving individual H I components within $|d\,v_c| \lesssim 150$ km s^{-1}, while the associated metal lines, such as the Mg II doublet, are resolved into seven discrete components in available optical Echelle spectra (see Boettcher et al., in preparation) for details.

Downloaded from https://academic.oup.com/mnras/article/497/1/498/5859973 by CNRS - ISTO user on 09 August 2022

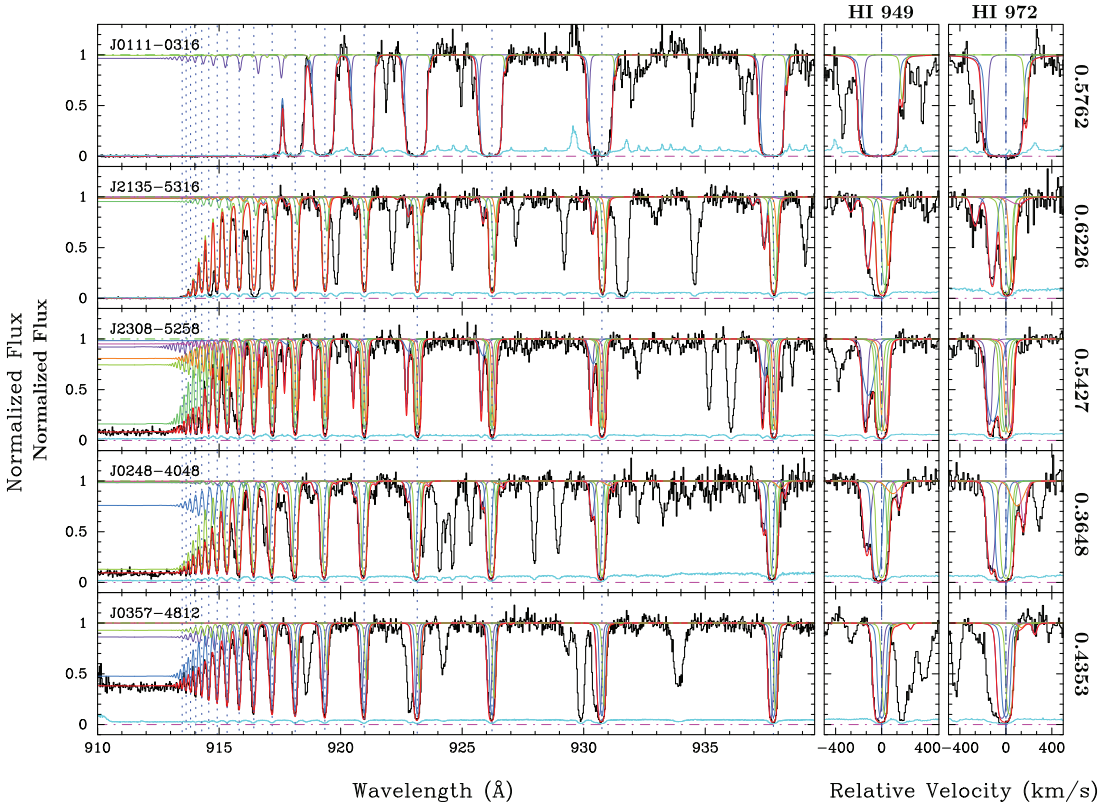

Figure 3. The Lyman series absorption spectra of the five new optically thick H I absorbers with $\tau_{912} \gtrsim 1$ found in the CUBS QSO sightlines. The absorbers are ordered with decreasing log N(H I) from top to bottom. The continuum-normalized spectra are shown in black with the corresponding 1σ error shown in cyan. The green and magenta dash–dotted lines mark the normalized continuum and zero flux levels for guidance. For each absorber, the velocity profiles of Ly δ (H I 949) and Ly γ (H I 972) are presented in the two right panels with zero velocity corresponding to the strongest H I component in Table 6. The remaining higher order Lyman series lines, along with the Lyman limit, are presented in the left panel with the vertical blue dotted lines indicating the expected positions of the Lyman transitions. The best-fitting Lyman series spectra are shown in red with individual components displayed in different colours.

the dominant H I component also corresponds to the strongest component observed in low-ionization transitions such as C II, N II, Mg II, and Si II. In particular, the associated Mg II components are fully resolved in the ground-based optical Echelle spectra. To facilitate direct comparisons between $N(H\,\mathrm{I})$ and ion abundances of different components, we also present initial measurements of Mg II component column densities, N_c(Mg II), in Table 6, but details regarding the Voigt profile analysis of metal absorption lines are presented in Zahedy et al. (in preparation). The best-fitting b_c(H I) of the dominant H I component ranges between $b_c(\mathrm{H\,I}) \approx 14$ km s^{-1} and $b_c(\mathrm{H\,I}) \approx 20$ km s^{-1}, with the exception of the H_2-bearing DLA at $z_{\rm abs} = 0.5762$ towards J0111−0316 for which the H I components are fully blended (see Boettcher et al., in preparation). Because $b_c(\mathrm{H\,I}) \equiv \sqrt{12.9^2\,T_4 + b_{\rm turb}^2}$ km s^{-1} for H I gas of temperature $T_{\rm gas} \equiv 10^4 \times T_4$ and turbulent width $b_{\rm turb}$, the best-fitting values constrain the underlying gas turbulence or bulk motion to be $b_{\rm turb} < 15$ km s^{-1} for optically thick absorbers of $T_{\rm gas} \sim 10^4$ K and still smaller for warmer temperatures.

4 DESCRIPTIONS OF INDIVIDUAL SYSTEMS

The LLS survey described in Section 3 has yielded five new LLSs at $z_{\rm abs} = 0.3640$–0.6226, including one damped Ly α absorber (DLA) which also contains molecular hydrogen (see Section 4.1 below). A suite of ionic transitions is detected in these high N(H I) absorbers, including low-ionization transitions such as C II, Mg II, Si II, and Fe II, and intermediate-ionization transitions such as C III and/or N III. With the exception of the H_2-bearing DLA, the other four LLSs also exhibit strong associated O VI doublets (Fig. 4). The observed relative column density ratios between low- and intermediate-ionization transitions indicate that the gas is ionized. Combining available galaxy survey data with known H I absorber properties provides new insights into the physical nature and origin of optically thick gas in galactic haloes (e.g. Chen, Kennicutt & Rauch 2005; Kacprzak, Murphy & Churchill 2010; Neeleman et al. 2016; Péroux et al. 2017; Rudie, Newman & Murphy 2017; Chen et al. 2019a, b; Mackenzie et al. 2019; Péroux et al. 2019; Lofthouse et al. 2020). Here, we summarize the absorption properties of the optically thick gas in descending order of the observed N(H I), as well as the galactic environment uncovered from available imaging and spectroscopic data. A detailed ionization analysis that accounts for the resolved component structure in the ionic transitions is presented in Zahedy et al. (in preparation).

4.1 The DLA at $z_{\rm abs} = 0.5762$ towards J0111−0316 near a massive, evolved galaxy at $d = 42$ pkpc

4.1.1 Absorption properties of the optically thick gas

The absorber at $z_{\rm abs} = 0.5762$ towards J0111−0316 is the strongest H I absorption system found in the LLS survey with $\tau_{912} > 6.6$. This absorber turns out to be a DLA of log $N(\mathrm{H\,I})/\mathrm{cm}^{-2} = 20.1^{+0.15}_{-0.05}$ with numerous features due to the H_2 Lyman–Werner bands also

Downloaded from https://academic.oup.com/mnras/article/497/1/498/5859973 by CNRS - ISTO user on 09 August 2022

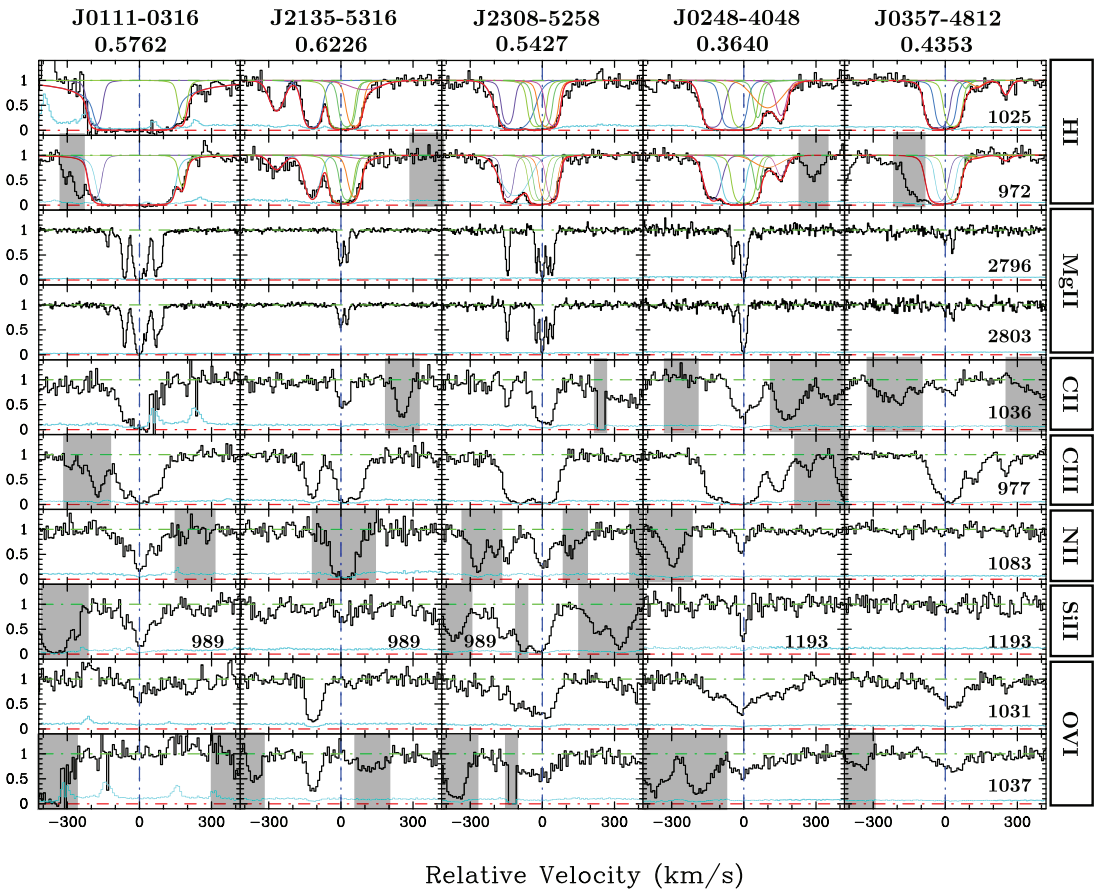

Figure 4. Absorption profiles of Ly β and Ly γ, and associated Mg II, C II, C III, N II, Si II, and O VI found in the LLSs presented in Fig. 3. The absorbers are ordered with decreasing log N(H I) from left to right. The rest-frame wavelength of each transition is listed in the lower-right corner of each panel in the right column. Following Fig. 3, zero velocity corresponding to the redshift of the strongest H I component in Table 6, 1σ errors are shown in cyan, and spectral regions that are contaminated with blended absorption features are greyed out for clarity. In particular, the position where the N II λ 1083 line is expected for the LLS at $z_{\rm abs} = 0.6226$ towards J2135−5316 is dominated by a strong Ly α absorber at $z_{\rm abs} = 0.4468$. The best-fitting Voigt profiles of Ly β and Ly γ lines, both separately for individual components (thin lines) and together for all components combined (thick red line), of each absorber are also reproduced in the two first rows for direct comparisons with resolved metal-line components.

detected in the COS spectrum. The large $N(H\,\mathrm{I})$ and the presence of H_2 indicate that the gas is primarily neutral. While low- and intermediate-ionization lines, including C II, Mg II, Si II, and C III are present, O VI is not detected with a 2σ upper limit to the O VI column density of log N(O VI)/cm^{-2} = 13.6. The observed column densities of different ions therefore provide a direct measurement of the underlying gas metallicity, which we found to be [M/H] = -0.5 ± 0.2, roughly 30 per cent of the solar value. Details regarding this system, both the absorption properties of the H_2-bearing DLA and its galactic environment, are presented in Boettcher et al. (in preparation).

In summary, the H I absorber exhibits a broad line width in the high-order Lyman series lines that led to a best-fitting $b_{\rm H\,I} \approx 49$ km s^{-1}. While N(H I) is well constrained by damping wings displayed in the Ly β profile, the broad $b_{\rm H\,I}$ is most likely driven by the unresolved H I component structure as indicated by the associated metal lines which are resolved into three dominant components at d$v_c = -60$, 0, +70 km s^{-1} (left-hand panel in Fig. 4). The components at d$v_c = -60$ and 0 km s^{-1} both exhibit associated H_2 absorption with a best-fitting H_2 column density of log $N(H_2)$/cm^{-2} = 15.6 ± 0.2 and 19.0 ± 0.1, respectively. Because the H I component structure is not resolved at the velocity separation between the two H_2 components, we calculate an integrated mean H_2 fraction of $f_{H_2} \equiv 2N(H_2)/[N(\mathrm{H\,I}) + 2\,N(H_2)] = 0.11 \pm 0.02$.

4.1.2 The galaxy environment

A group of nine galaxies of r-band magnitude $AB(r) = 20.4-24$ mag has been spectroscopically identified with Magellan at projected distance $d < 600$ pkpc and line-of-sight velocity interval d$v_{\rm gal} < 300$ km s^{-1} from the H_2-bearing DLA. The closest galaxy is identified at $d = 42$ pkpc and d$v_{\rm gal} = -57$ km s^{-1} from the DLA and it is bright with $AB(r) = 21.47$, corresponding to $\approx$1.9 L_* at $z = 0.576$ (see e.g. Cool et al. 2012). Both the broad-band photometric colours and the optical spectrum of the closest galaxy indicate that it is an evolved galaxy of stellar mass $M_{\rm star} = 8 \times 10^{10}$ M$_\odot$ and no trace of on-going star formation with a 2σ upper limit on the star formation rate (SFR) of SFR < 0.2 M$_\odot$ yr^{-1}. Two more galaxies are found at $d < 300$ pkpc. Both are sub-L_* galaxies with log $M_{\rm star}$/M$_\odot$ = 9.4 and 9.9 at $d = 130$ and 167 pkpc, respectively. This represents one of two H_2 absorbers found in the vicinity of a massive, evolved galaxy beyond the nearby Universe (see Zahedy et al., in preparation, for a second case, and Muzahid, Srianand & Charlton 2015; Muzahid et al. 2016 for a list of H_2 absorbers found in the vicinities of star-forming galaxies).

Downloaded from https://academic.oup.com/mnras/article/497/1/498/5859973 by CNRS - ISTO user on 09 August 2022

Table 6. Summary of best-fitting Voigt profile parameters of new $\tau_{912} \gtrsim 1$ absorbers.[a]

No.	dv_c (km s^{-1})	log N_c(H I)/cm^{-2}	b_c(H I) (km s^{-1})	log N_c(Mg II)/cm^{-2}
	J0111−0316 $z_{\rm abs} = 0.57616$, log N(H I)/cm^{-2} = 20.1 ± 0.1[b]			
1	−186	15.8 ± 0.05	15^{+1}_{-2}	<11.1
2	−16	$20.10^{+0.15}_{-0.05}$	49^{+0}_{-1}	>14.0
3	+178	14.9 ± 0.1	11^{+4}_{-3}	<11.1
	J2135−5316, $z_{\rm abs} = 0.62255$, log N(H I)/cm^{-2} = 18.01 ± 0.04			
1	$-268.3^{+2.3}_{-2.6}$	$14.51^{+0.03}_{-0.04}$	$32.5^{+2.7}_{-2.6}$	<11.0
2	$-119.7^{+0.5}_{-0.7}$	15.38 ± 0.02	26.8 ± 0.6	<11.0
3	0.0	18.00 ± 0.04	18.7 ± 0.2	12.76 ± 0.01
4	+26.4	$15.87^{+0.10}_{-0.38}$	$18.5^{+3.7}_{-2.8}$	12.53 ± 0.01
5	$+55.5^{+3.6}_{-8.4}$	$15.32^{+0.22}_{-0.11}$	$21.9^{+4.5}_{-1.8}$	<11.0
6	$+98.0^{+14.3}_{-13.4}$	$14.17^{+0.10}_{-0.16}$	$83.0^{+17.9}_{-14.3}$	<11.0
	J2308−5258, $z_{\rm abs} = 0.54273$, log N(H I)/cm^{-2} = 17.59 ± 0.02			
1	−144.4	16.12 ± 0.03	$12.2^{+0.8}_{-0.6}$	12.96 ± 0.02
2	−114.3 ± 3.1	15.44 ± 0.02	$59.6^{+3.3}_{-3.0}$	<11.1
3	−23.9	$16.67^{+0.03}_{-0.05}$	$16.1^{+0.6}_{-0.5}$	12.98 ± 0.04
4	0.0	17.46 ± 0.02	$14.4^{+1.0}_{-0.7}$	13.46 ± 0.05
5	+23.9	$16.53^{+0.06}_{-0.10}$	18[c]	13.13 ± 0.10
6	+42.3	15.90 ± 0.08	$15.7^{+1.5}_{-1.2}$	12.90 ± 0.01
	J0248−4048, $z_{\rm abs} = 0.36400$, log N(H I)/cm^{-2} = 17.57 ± 0.01			
1	$-130.8^{+1.2}_{-1.0}$	15.42 ± 0.02	$31.1^{+1.2}_{-0.8}$	<11.3
2	−42.1	16.64 ± 0.02	$23.8^{+0.5}_{-0.7}$	12.55 ± 0.03
3	0.0	17.51 ± 0.01	20.0 ± 0.3	13.44 ± 0.03
4	$+57.3^{+1.2}_{-1.6}$	15.36 ± 0.04	$9.3^{+1.5}_{-1.0}$	<11.3
5	$+100.0^{+8.4}_{-10.1}$	14.70 ± 0.08	$69.0^{+6.1}_{-5.6}$	<11.3
6	$+154.4^{+1.5}_{-1.6}$	14.59 ± 0.05	$19.2^{+2.3}_{-1.7}$	<11.3
	J0357−4812, $z_{\rm abs} = 0.43527$, log N(H I)/cm^{-2} = 17.18 ± 0.01			
1	−35.5	16.37 ± 0.02	$24.2^{+0.4}_{-0.3}$	11.47 ± 0.16
2	0.0	17.07 ± 0.01	17.4 ± 0.5	12.10 ± 0.05
3	+31.4	16.07 ± 0.03	18.8 ± 0.5	12.38 ± 0.11
4	+85.8 ± 3.5	$13.55^{+0.10}_{-0.14}$	13.4 ± 2.8	<11.3
5	$+133.1^{+3.7}_{-4.9}$	$13.60^{+0.07}_{-0.06}$	$27.9^{+3.7}_{-2.8}$	<11.3
6	$+251.7^{+2.1}_{-1.7}$	$13.89^{+0.07}_{-0.06}$	$16.2^{+2.1}_{-2.0}$	<11.3

[a]Best-fitting velocity centroid dv_c of individual components relative to $z_{\rm abs}$, H I component column density N_c(H I) and Doppler parameter b_c, and Mg II component column density N_c(Mg II) from Zahedy et al. (in preparation).
[b]Because the primary H I components are not resolved, N_c(Mg II) here represents the sum of all seven resolved components in the optical Echelle spectrum and $dv_c = 0$ km s^{-1} corresponds to the strongest Mg II component. See Boettcher et al. (in preparation) for details.
[c]Due to heavy blending with adjacent H I components, the b value is fixed to the expected thermal value for the temperature determined from the corresponding Mg II component.

4.2 The LLS at $z_{\rm abs} = 0.6226$ towards J2135−5316 in a massive galaxy group at $d_{\rm group} = 177$ pkpc

4.2.1 Absorption properties of the optically thick gas

The LLS at $z_{\rm abs} = 0.6226$ towards J2135−5316 has $\tau_{912} > 6.3$. It is the second strongest LLS found in our sample (after the H_2-bearing DLA towards J0111−0316), and is resolved into a minimum of six components with ≈99 per cent of the N(H I) contained in the central component at $dv_c = 0$ km s^{-1} (component 3 in Table 6 for this system) and ≈1 per cent contained in the components at $dv_c = -120$, +26, and +56 km s^{-1} (components 2, 4, and 5, respectively, in Table 6). The remaining components contribute negligibly to the total N(H I), but they dominate the line width observed in the first few Lyman lines at $dv_c = -268$ km s^{-1} and $dv_c = +98$ km s^{-1} (Figs 3 and 4). In particular, the large b value of component 6 ($b_c \approx 83$ km s^{-1} and log N_c(H I)/cm^{-2} ≈ 14.2) in Table 6 is likely due to blended weak H I components that are not resolved in the COS spectra, but are necessary for explaining the observed Ly α and Ly β line profiles. This component is not present in higher order Lyman lines and the lack of resolving power has a negligible impact on the total N(H I) measurement, but the best-fitting N_c(H I) for component 6 should be taken with caution.

While low-ionization species are concentrated in the two strongest H I components at $dv_c = 0$ and +26 km s^{-1} (components 3 and 4 in Table 6), intermediate ions exhibit matching component structure with the first few Lyman series lines at $-120 \lesssim dv_c \lesssim 60$ km s^{-1}. In particular, component 2 at $dv_c = -120$ km s^{-1} exhibits strong and relatively narrrow C III and O VI absorption and no detectable low-ionization transitions, showing a distinct ionization state from components 3 and 4).

4.2.2 The galaxy environment

The MUSE observations of this field presented in Section 2.4 have uncovered 86 objects in the 1 arcmin × 1 arcmin field of view with pseudo r-band magnitude ranging from $AB(r) = 21$ to 26.6 mag, in addition to a bright star and the QSO. Robust redshift measurements are obtained for 46 of these objects (left-hand panel of Fig. 5). Comparing the photometric measurements of common objects observed in both MUSE and DES shows that the pseudo r-band magnitudes are consistent with DES r-band measurements to within 0.1 magnitude uncertainties. The spectroscopic survey is 100 per cent, >90 per cent, and 75 per cent complete for objects brighter than $AB(r) = 23$, 24, and 25 mag, respectively. Redshift measurements are made using a χ^2 fitting routine that compares the observed spectrum with models formed from a linear combination of four eigenspectra from the SDSS at different redshifts (see Chen & Mulchaey 2009; Johnson, Chen & Mulchaey 2013, for a detailed description). The best-fitting redshift of each object was visually inspected for confirmation. The redshifts of spectroscopically identified galaxies range from $z_{\rm gal} = 0.24$ to $z = 4.49$.

A group of 10 galaxies is found in the vicinity of the LLS with pseudo r-band magnitude ranging from $AB(r) = 21.2$ to 24.7 mag and line-of-sight velocity offset ranging from $dv_{\rm gal} = -499$ km s^{-1} to $dv_{\rm gal} = +184$ km s^{-1} (Fig. 5). The remaining spectroscopically identified galaxies in the MUSE field all appear at a cosmologically distinct redshift with a velocity separation exceeding $|dv_{\rm gal}| = 600$ km s^{-1} from the LLS. The galaxies in the LLS-associated group span a range in angular distance from $\theta = 10.6$ arcsec to $\theta = 38.1$ arcsec, corresponding to a range in projected distance from $d = 72$ to 252 pkpc at the redshift of the LLS. Optical spectra of the members of the LLS-associated galaxy group are presented in Fig. 6 with increasing projected distance from top to bottom, which clearly show a wide range in the star formation histories among the members of the galaxy group. A detailed analysis of galaxy properties is presented in Appendix A. In summary, we estimate its intrinsic r-band absolute magnitude M_r based on the observed $AB(r)$ and find that the group galaxies span a range in M_r from $M_r = -22.5$ (or 3 L_*) for a post-starburst/AGN at $d = 244$ pkpc (see

Downloaded from https://academic.oup.com/mnras/article/497/1/498/5859973 by CNRS - ISTO user on 09 August 2022

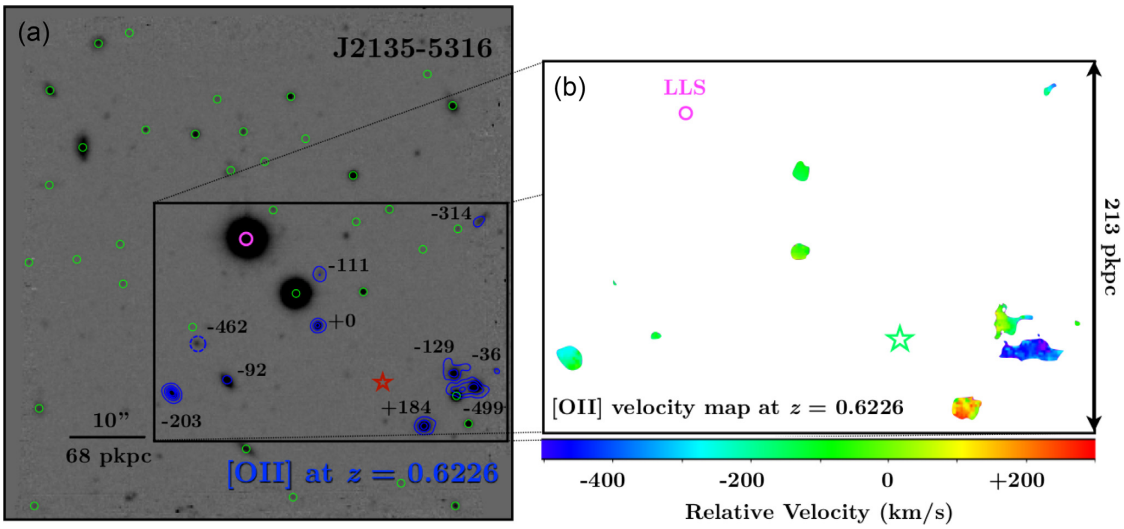

Figure 5. The galaxy environment uncovered by MUSE for the LLS at $z_{\rm abs} = 0.6226$ towards J2135−5316. The pseudo *r*-band image from Fig. 2 is reproduced in panel (*a*). North is up and east is to the left. Objects that are spectroscopically identified at cosmologically distinct redshifts from the LLS are marked by green circles, while galaxies spectroscopically identified in the vicinity of the LLS are highlighted by their blue [O II] emission contours of constant surface brightness 0.25, 1.25, 2.5, 3.7, and 5×10^{-17} erg s^{-1} cm^{-2} arcsec^{-2} and marked by their line-of-sight velocity offset (km s^{-1}) from $z_{\rm abs} = 0.6226$. The galaxy at $\Delta v = -462$ km s^{-1} exhibits only a faint trace of [O II] emission, with surface flux density below the lowest contour. It is marked by a blue, dashed circle. A group of 10 galaxies is found in the vicinity of the LLS with angular distance ranging from $\theta = 10.6$ to 38.1 arcsec from the QSO sightline (magenta circle), corresponding to a range in projected distance from $d = 72$ to 252 pkpc at the redshift of the LLS. The light-weighted centre of the galaxy group is marked by an open star symbol at (−17.9, −19.0 arcsec) from the QSO sightline. The line-of-sight velocity map of [O II] emission is presented in the right-hand panel with zero velocity corresponding to $z_{\rm abs} = 0.6226$. The location of the LLS is marked by an open magenta circle. The galaxy group spans a range in the line-of-sight velocity offset from $\mathrm{d}v_{\rm gal} = -499$ km s^{-1} to $\mathrm{d}v_{\rm gal} = +184$ km s^{-1} from the absorber with a light-weighted centre at $\mathrm{d}v_{\rm gal} = -170$ km s^{-1} (open star symbol in panel *b*). While the galaxy group members all exhibit an ordinary continuum morphology in the pseudo *r*-band image, the [O II] contours revealed spatially extended line-emitting nebulae around the two massive group members at $\mathrm{d}v_{\rm gal} = -129$ and −499 km s^{-1} in the lower-right corner, suggesting strong interactions between the two galaxies. The galaxy at $\mathrm{d}v_{\rm gal} = -499$ km s^{-1} is also the most massive member of the group with spectral features indicative of a post-starburst phase (and possibly hosting an AGN; see the text for details).

Appendix A) to $M_r = -18.3$ (or 0.06 L_*) for a faint dwarf at $d = 252$ pkpc and $\mathrm{d}v_{\rm gal} = -36$ km s^{-1}. In addition, we estimate $M_{\rm star}$ based on the rest-frame $g-r$ colour inferred from the MUSE spectra and the prescription of Johnson et al. (2015), and find log $M_{\rm star}/\mathrm{M}_\odot =$ 8.6–11.2 for these galaxies. The observed and derived properties of the galaxies, including best-fitting redshift $z_{\rm gal}$, projected distance d, mean line-of-sight velocity offset $|\mathrm{d}v_{\rm gal}|$, pseudo *r*-band magnitude $AB(r)$, intrinsic absolute *r*-band magnitude M_r, inferred total stellar mass $M_{\rm star}$, galaxy type, The total integrated [O II] line flux, and unobscured SFR are summarized in columns (2) through (10) of Table 7.

The available MUSE data show that while the closest galaxy to the LLS is a 0.12 L_* galaxy with $M_{\rm star} \approx 7.9 \times 10^8$ M$_\odot$ at $d =$ 72 pkpc and $\mathrm{d}v_{\rm gal} = -111$ km s^{-1}, it is likely part of a dynamic group containing several members that are 100 times more massive at <200 pkpc away. All 10 galaxies contribute to a total stellar mass of $M_{\rm star} \approx 3.4 \times 10^{11}$ M$_\odot$ with ≈60 per cent contained in the interacting pair. We calculate a light-weighted centre located at (−17.9, −19.0 arcsec) from the QSO sightline (open star symbol in Fig. 5). The corresponding projected distance of the 'group' is therefore $d_{\rm group} = 177$ pkpc and the light-weighted line-of-sight velocity offset is $\mathrm{d}v_{\rm group} \approx -170$ km s^{-1} between the galaxy 'group' and the LLS. We also calculate a line-of-sight velocity dispersion of $\sigma_{\rm group} = 211$ km s^{-1}, implying a dynamical mass of $M_{\rm dyn} \approx 1.1 \times 10^{13}$ M$_\odot$ and a virial radius of $r_{\rm vir} \approx 360$ kpc for the galaxy group. The strong LLS may be due to gaseous streams at $\gtrsim 0.5\, r_{\rm vir}$ in the intragroup medium (e.g. Chen et al. 2019b).

4.3 The LLS at $z_{\rm abs} = 0.5427$ towards J2308−5258 near a star-forming galaxy at $d = 32$ pkpc

4.3.1 Absorption properties of the optically thick gas

The LLS at $z_{\rm abs} = 0.5427$ towards J2308−5258 has $\tau_{912} = 2.53 \pm 0.01$. It is resolved into a minimum of six components with ≈74 per cent of N(H I) contained in the central component (component 4 in Table 6) at $\mathrm{d}v_c = 0$ km s^{-1} and ≈21 per cent contained in the two components at $\mathrm{d}v_c = -24$ and +24 km s^{-1} (components 3 and 5, respectively, in Table 6). Different from previous systems, the remaining components, in particular components 1 and 6, contribute an appreciable amount (3 per cent and 2 per cent, respectively) to the total N(H I) (Figs 3 and 4). However, the large b value of component 2 ($b_c \approx 60$ km s^{-1} and log N_c(H I)/cm^{-2} ≈ 15.4) in Table 6 is likely due to unresolved H I components in the COS spectra, but is necessary for explaining the observed Ly α and Ly β line profiles. Because this component is not present in higher order Lyman lines, the lack of resolving power has a negligible impact (<1 per cent) on the total N(H I) measurement but the best-fitting N_c(H I) for component 2 should be taken with caution.

There is a good one-to-one correspondence between the associated low-ionization transitions and the H I components with the only exception being component 2, the broad component at $\mathrm{d}v_c \approx -114$ km s^{-1}. The kinematic profiles of low ions also match well with those of intermediate- and highly ionized species. However, it is clear that these components exhibit distinct N(H I) to N(Mg II) ratios. Specifically, components 1 and 3 exhibit a column density ratio of 2:7 in N(H I), while the associated Mg II components

Downloaded from https://academic.oup.com/mnras/article/497/1/498/5859973 by CNRS - ISTO user on 09 August 2022

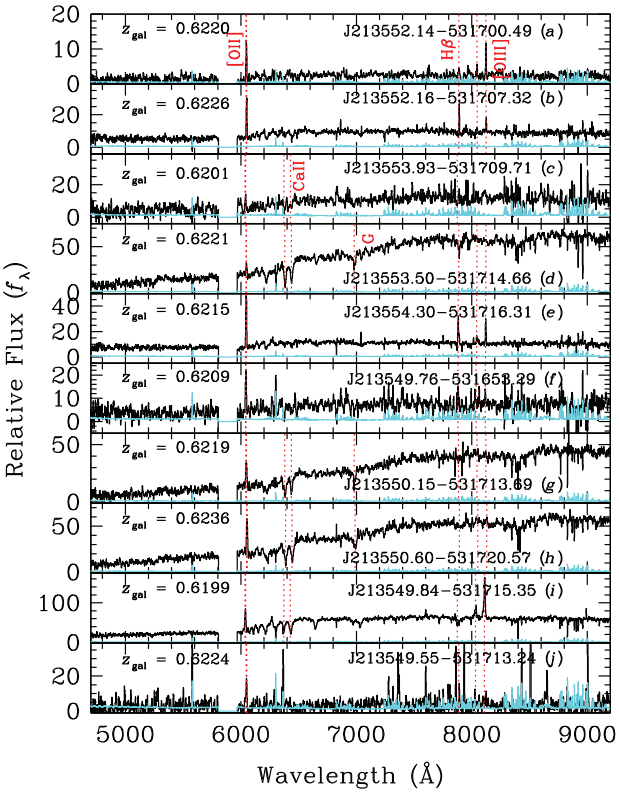

Figure 6. Optical spectra of a group of 10 galaxies identified in the vicinity of the LLS at $z_{\rm abs} = 0.6226$ towards J2135−5258 from MUSE observations. The corresponding 1σ error spectra are shown in cyan. The spectra are ordered with increasing projected distance of the galaxies from $d = 72$ pkpc at the top to $d = 252$ pkpc at the bottom. Galaxies in the group exhibit a wide range in star formation history with the most luminous and massive members displaying prominent absorption features such as Ca II and *G*-band (panels *d*, *g*, and *h*), indicative of evolved old stars, one galaxy displaying a strong Balmer absorption series with weak H β and [O II] (panel *i*), indicative of a post-starburst phase, and the rest displaying strong [O II] emission and no significant Ca II absorption (panels *a*, *b*, *e*, *f*, and *j*), indicating a predominantly young stellar population. The galaxy at $z_{\rm gal} = 0.6199$ (panel *i*) also exhibits [Ne III] and a high [O III]/H β line ratio, suggesting the presence of an AGN.

exhibit a comparable strength. The differential N(Mg II)/N(H I) ratios strongly imply differences in the underlying gas metallicity between these components (e.g. Zahedy et al. 2019). Different from the LLS at $z = 0.6226$ towards J2135−5316, the O VI doublet of this LLS is broad and covers the velocity range of all lower ionization species, highlighting the multiphase nature of the gas.

4.3.2 *The galaxy environment*

The MUSE observations of this field are ongoing. Only a third of the observations have been executed. It is expected that the data will reach a comparable depth as seen in J0357−4812 (see Section 4.5 below). An initial analysis of the data collected so far has revealed a luminous disc galaxy of $AB(r) \approx 21$ mag at $z_{\rm gal} = 0.5426$ and $\theta = 5.1$ arcsec from the QSO sightline, corresponding to $d = 32$ pkpc and $dv_{\rm gal} = -19$ km s^{-1} from the LLS. At $z = 0.54$, the observed pseudo *r*-band magnitude implies $M_r \approx -22.1$ (or 2.1 L_*) and log $M_{\rm star}/{\rm M}_\odot \approx 10.9$. Similar to the LLS-absorbing galaxy in J0357−4812 (see Section 4.5 and Fig. 11), the optical spectrum of this galaxy is characterized by a combination of strong Ca II H&K absorption and strong [O II] and H β emission lines (Fig. 7). Different from the configuration between the QSO probe and the LLS absorbing galaxy in J0357−4812, the QSO here probes the diffuse gas at ≈28° from the minor axis of the inclined disc. While no other galaxies are found in the vicinity of the LLS to $AB(r) \approx 25.5$ mag, suggesting that the luminous galaxy at $d = 32$ pkpc is singularly responsible for the LLS, the survey is still incomplete. A detailed analysis of the galactic environment of this LLS will be presented in a later paper when complete galaxy survey data are available from MUSE and Magellan.

4.4 The LLS at $z_{\rm abs} = 0.3640$ towards J0248−4048 near a pair of low-mass dwarfs at $d \approx 26$ pkpc

4.4.1 *Absorption properties of the optically thick gas*

The LLS at $z_{\rm abs} = 0.3640$ towards J0248−4048 has $\tau_{912} = 2.48 \pm 0.01$. It is resolved into a minimum of six components with ≈87 per cent of N(H I) contained in the central component at $dv_c = 0$ km s^{-1} and ≈12 per cent contained in the component at $dv_c = -42$ km s^{-1} (components 3 and 2, respectively, in Table 6). The remaining components contribute no more than 1 per cent to the total $N(H\,{\rm I})$, but they dominate the line width observed in the first few Lyman lines with velocity ranging from $dv_c = -131$ km s^{-1} to $dv_c = +154$ km s^{-1} (Figs 3 and 4). The large *b*-value of component 5 ($b_c \approx 69$ km s^{-1} and log N_c(H I)/cm$^{-2} \approx 14.7$) in Table 6 is likely due to blended weak H I components that are not resolved in the COS spectra, but is necessary for explaining the observed Ly α and Ly β line profiles. Similar to component 6 of the LLS towards J2135−5316, this component is not present in higher order Lyman lines and the lack of resolving power has a negligible impact on the total N(H I) measurement. However, the best-fitting N_c(H I) for component 5 should be taken with caution.

While low-ionization species are concentrated in the two strongest H I components at $dv_c = -42$ and 0 km s^{-1} (components 2 and 3 in Table 6), intermediate ions exhibit a matching component structure with the first few Lyman series lines. In addition, the highly ionized species traced by the O VI doublet exhibit a broader line profile encompassing all lower ionization species, revealing a multiphase nature of the LLS.

4.4.2 *The galaxy environment*

The MUSE observations of this field presented in Section 2.4 provide a deep view of the line-of-sight galaxy properties. We have uncovered 67 objects in the MUSE field of view with pseudo *r*-band magnitude ranging from $AB(r) = 20.5$ to 26.9 mag in addition to the QSO. Of the 30 objects brighter than $AB(r) = 25$ mag, we are able to determine a robust redshift for 28, reaching a survey completeness of >90 per cent. The redshifts of spectroscopically identified galaxies in the MUSE field around J0248−4048 range from $z_{\rm gal} = 0.21$ to $z_{\rm gal} = 1.46$. Three galaxies are found in the vicinity of the LLS with line-of-sight velocity offset $|dv_{\rm gal}| < 70$ km s^{-1} (Fig. 8). The remaining spectroscopically identified galaxies in the MUSE field all appear at a cosmologically distinct redshift with a velocity separation exceeding $|dv_{\rm gal}| = 1000$ km s^{-1} from the LLS. The angular distances of the three LLS-associated galaxies are $\theta = 3.0$, 7.8, and 29.7 arcsec, corresponding to $d = 15$, 37, and 150 pkpc, respectively, at the redshift of the LLS.

The extracted MUSE spectra of the three LLS-associated galaxies are presented in Fig. 9 with increasing projected distance from top to bottom. All three galaxies exhibit strong nebular emission lines, including [O II], H β, [O III], and H α, commonly seen in star-forming regions, and they are of low mass with faint traces of continuum emission. Details regarding the properties of these low-mass dwarfs

Downloaded from https://academic.oup.com/mnras/article/497/1/498/5859973 by CNRS - ISTO user on 09 August 2022

Table 7. Intrinsic properties of galaxies in the vicinity of an LLS.

Galaxy (1)	$z_{\rm gal}$ (2)	d (pkpc) (3)	$dv_{\rm gal}$[a] (km s^{-1}) (4)	$AB(r)$ (5)	M_r[b] (6)	log $M_{\rm star}/M_\odot$ (7)	Type[c] (8)	$f_{\rm line}$[d] (10^{-17} erg s^{-1} cm^{-2}) (9)	SFR[e] ($M_\odot$ yr^{-1}) (10)	ISM (O/H)[f] (11)
Galaxies associated with the LLS at $z_{\rm abs} = 0.6226$ towards J2135−5258										
J213552.14−531700.49	0.6220	72	−111	24.0	−19.0	8.9	SF	2.06 ± 0.03	0.22	–
J213552.16−531707.32	0.6226	100	0	22.6	−20.4	9.4	SF	3.77 ± 0.04	0.40	–
J213553.93−531709.71	0.6201	104	−462	23.7	−20.0	10.2	A	0.05 ± 0.01	0.01	–
J213553.50−531714.66	0.6221	129	−92	21.6	−22.0	10.7	A	0.64 ± 0.08	0.07	–
J213554.30−531716.31	0.6215	154	−203	22.3	−20.7	9.6	SF	1.14 ± 0.05	0.12	–
J213549.76−531653.29	0.6209	211	−314	23.0	−20.0	9.3	SF	1.00 ± 0.03	0.11	–
J213550.15−531713.69	0.6219	222	−129	21.8	−21.9	10.6	A	4.96 ± 0.16	0.53	–
J213550.60−531720.57	0.6236	231	+184	21.5	−22.2	10.8	A	6.47 ± 0.30	0.69	–
J213549.84−531715.35	0.6199	244	−499	21.2	−22.5	11.2	PSB	15.23 ± 0.72	1.63	–
J213549.55−531713.24	0.6224	252	−36	24.7	−18.3	8.6	SF	0.26 ± 0.02	0.03	–
Galaxy associated with the LLS at $z_{\rm abs} = 0.5427$ towards J2308−5258[g]										
J230837.42−525845.07	0.5426	32	−19	21.0	−22.1	10.9	SF+A	–	–	–
Galaxies associated with the LLS at $z_{\rm abs} = 0.3640$ towards J0248−4048										
J024806.09−404835.64	0.3638	15	−44	–	–	–	SF	4.41 ± 0.03	0.11	7.7
J024805.69−404831.04	0.3639	37	−22	25.1	−16.3	7.8	SF	0.63 ± 0.02	0.01	7.5
J024803.87−404822.24	0.3637	150	−66	24.1	−17.3	8.2	SF	1.98 ± 0.02	0.05	7.6
Galaxy associated with the LLS at $z_{\rm abs} = 0.4353$ towards J0357−4812										
J035723.07−481215.78	0.4358	67	+105	20.7	−21.7	10.4	SF+A	6.14 ± 0.06	0.28	–

[a]Line-of-sight velocity offset relative to the strongest H I absorbing component at $z_{\rm abs}$.
[b]At $z = 0.3$, star-forming galaxies (SF) have a characteristic rest-frame absolute r-band magnitude of $M_{r_*} = -21.3$ and evolved galaxies (A) have $M_{r_*} = -21.5$ (e.g. Cool et al. 2012).
[c]SF: emission-line dominated star-forming; PSB: post-starburst; A: absorption-dominated evolved galaxies.
[d]Integrated line flux for H α at $z < 0.4$ and [O II] at higher redshifts.
[e]Unobscured SFR inferred from the integrated line flux reported in column (9) without dust extinction corrections. The conversion from H α is based on the calibrator of Kennicutt & Evans (2012), while the conversion from [O II] is taken from Kewley, Geller & Jansen (2004). For galaxies at $z < 0.4$, the observed H α/H β ratio indicates that the dust-extinction corrected SFR should be about between 24 per cent and 100 per cent higher (see Section 4.2 for discussion).
[f]Uncertainties are driven by the R_{23} calibration error and are estimated to be about 0.1 dex. For comparison, the oxygen abundance of the Sun is $12 + \log({\rm O/H})_\odot = 8.69 \pm 0.05$ (Asplund et al. 2009).
[g]MUSE observations are on-going. Available partial data are sufficient for identifying a luminous galaxy in the vicinity of the LLS. A full analysis is deferred to a later paper when the observations have been completed.

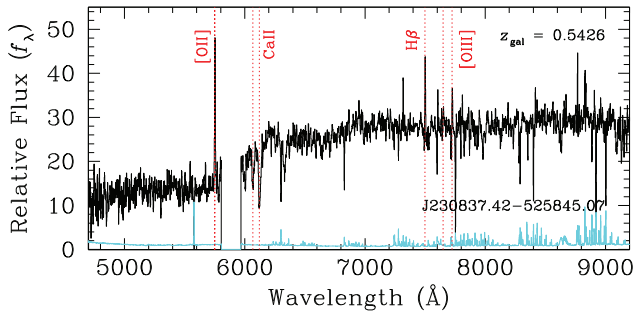

Figure 7. Optical spectrum of a luminous galaxy identified in the vicinity of the LLS at $z_{\rm abs} = 0.5427$ towards J2308−5258 from available MUSE data. The corresponding 1σ error spectrum is shown in cyan. The galaxy is bright and the spectrum exhibits prominent absorption features due to Ca II H&K and the Balmer series, along with strong [O II] and H β emission lines (highlighted in red dotted lines with corresponding line identifications).

are presented in Appendix B. In summary, the galaxies have low luminosity, $\lesssim 0.03\,L_*$, and low mass, log $M_{\rm star}/{\rm M}_\odot \lesssim 8.2$, with an unobscured SFR in the range of 0.01–0.11 $M_\odot$ yr^{-1} and a gas-phase metallicity in their interstellar medium (ISM) of ≈10 per cent solar. The observed and derived properties of the galaxies are shown in columns (2) through (11) of Table 7.

While both the relative line-of-sight velocity offsets and projected separations of the three low-mass dwarf galaxies are small with $|dv_{\rm gal}| < 50$ km s^{-1} and $d \lesssim 150$ pkpc to the LLS, the observed low stellar mass also implies a low-mass host dark matter halo. If no massive galaxies are found in the ongoing *shallow and wide* survey beyond the MUSE field of view, then the low-mass dwarf at $d = 150$ pkpc may be too far away to be sharing a common dark matter halo with the two galaxies at $d < 40$ pkpc. Indeed, adopting a range of the stellar mass to dark matter halo mass ratio for low-mass dwarfs from Miller et al. (2014) and Read et al. (2017), we infer a dark matter halo mass of log $M_h \approx 9.8$–10.6 for the galaxy at $d = 150$ pkpc and a corresponding virial radius of $r_{\rm vir} \approx 35$−65 kpc. The LLS along the QSO sightline would be at a distance more than $2 \times r_{\rm vir}$ from the galaxy at $d = 150$ pkpc. We therefore conclude that the LLS is most likely associated with a pair of low-mass dwarfs at $d = 15$ and 37 pkpc, respectively, with an ISM metallicity of ≈10 per cent solar (see Section 5.3 below for further discussion).

4.5 The LLS at $z_{\rm abs} = 0.4353$ towards J0357−4812 near a rotating disc galaxy at $d = 67$ pkpc

4.5.1 Absorption properties of the optically thick gas

The LLS at $z_{\rm abs} = 0.4353$ towards J0357−4812 has $\tau_{912} = 0.99 \pm 0.01$. It is resolved into a minimum of six components with $\gtrsim$99 per cent of N(H I) contained in the central three components

Downloaded from https://academic.oup.com/mnras/article/497/1/498/5859973 by CNRS - ISTO user on 09 August 2022

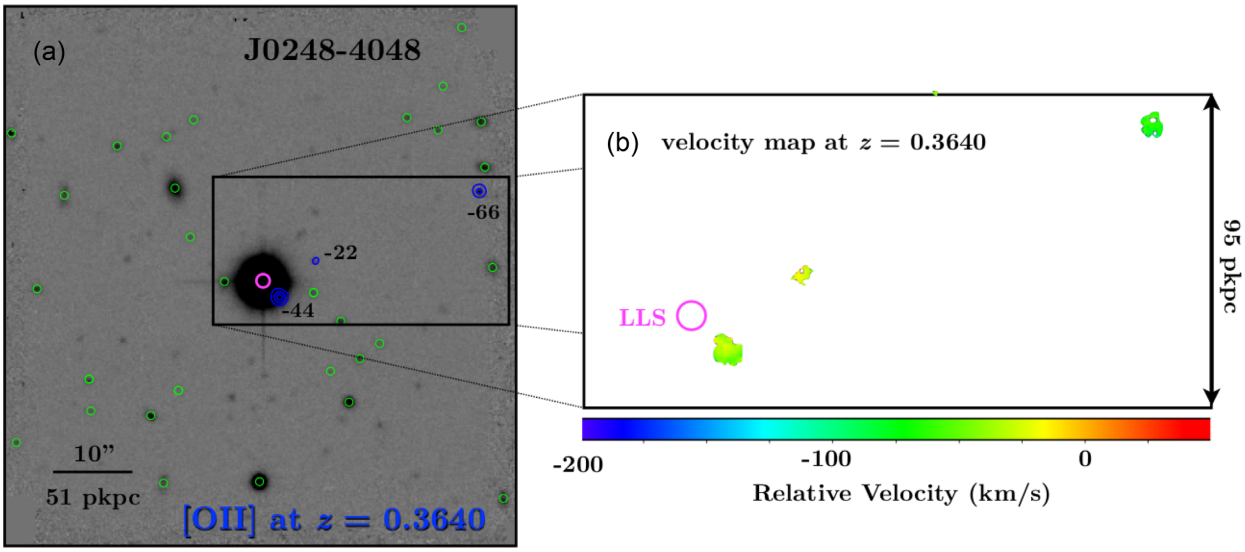

Figure 8. The galaxy environment uncovered by MUSE for the LLS at $z_{\rm abs} = 0.3640$ towards J0248−4048. The pseudo *r*-band image from Fig. 2 is reproduced in panel (*a*). North is up and east is to the left. Objects that are spectroscopically identified at a cosmologically distinct redshift from the LLS are marked by green circles, while galaxies associated with the LLS are highlighted by blue [O II] emission contours of constant surface brightness 0.25, 1.25, and 2.5×10^{-17} erg s^{-1} cm^{-2} arcsec^{-2} and marked by the line-of-sight velocity offset (km s^{-1}) from $z_{\rm abs} = 0.3640$. Three galaxies are found in the vicinity of the LLS with angular distance of $\theta = 3.0$, 7.8, and 29.7 arcsec from the QSO sightline (magenta circle), corresponding to $d = 15$, 37, and 150 pkpc, respectively, at the redshift of the LLS. The line-of-sight velocity map based on a simultaneous fit to the observed [O II] doublet, H β, [O III]$\lambda\lambda$ 4960, 5008, and H α (see Fig. 9) is presented in the right-hand panel with zero velocity corresponding to $z_{\rm abs} = 0.3640$. The location of the LLS is marked by an open magenta circle. All three LLS-associated galaxies are found at relatively small line-of-sight velocity offset of $|\Delta\, v| < 70$ km s^{-1} from the absorber.

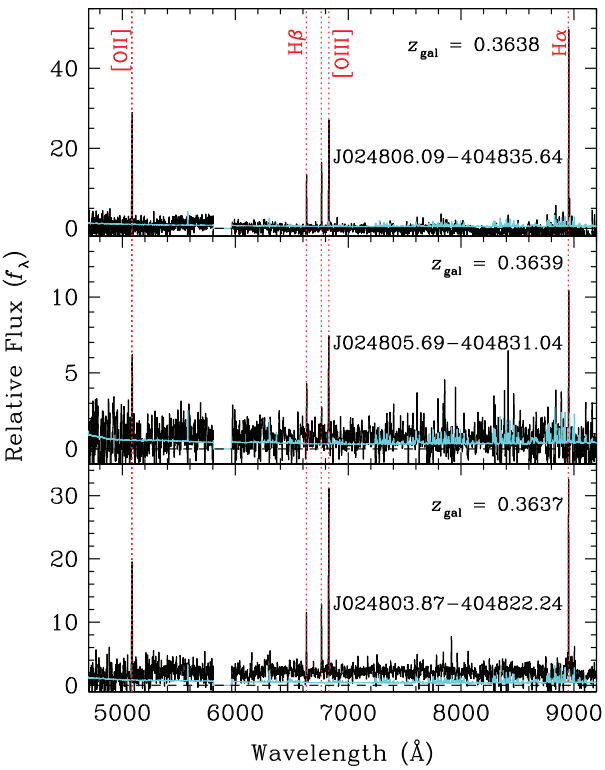

Figure 9. Optical spectra of three galaxies identified in the vicinity of the LLS at $z_{\rm abs} = 0.3640$ towards J0248−4048 from MUSE observations. The corresponding 1σ error spectra are shown in cyan. The spectra are ordered with increasing projected distance from top to bottom, at $d = 15$, 37, and 150 pkpc, from the QSO sightline. All three galaxies exhibit an emission-line dominated spectrum. Prominent spectral features are highlighted in red dotted lines, marked with the corresponding line identifications.

at $|{\rm d}v_c| < 40$ km s^{-1} (components 1 through 3 in Table 6). The remaining components contribute negligibly to the total N(H I), but are necessary for explaining the observed line profiles of the first few Lyman lines with velocity ranging from ${\rm d}v_c = 86$ km s^{-1} to ${\rm d}v_c = +252$ km s^{-1} (Figs 3 and 4).

Fig. 4 shows that the component at ${\rm d}v_c = +31.4$ km s^{-1} (component 3 of this LLS in Table 6) exhibits the strongest metal absorption, while containing only ≈8 per cent of the total N(H I). Specifically, components 2 and 3 exhibit a column density ratio of 10:1 in N(H I), but 4:9 in N(Mg II). This differential absorption strength between H I and associated ionic transitions of components 2 and 3 applies to all ions observed from low- to high-ionization species, strongly implying a difference in the underlying gas metallicity (e.g. Prochter et al. 2010; Zahedy et al. 2019). Similar to the LLSs towards J2308−5258 and J0248−4048, the highly ionized species traced by the O VI doublet exhibit a broad line profile encompassing all lower ionization species, indicating a multiphase nature of the LLS.

4.5.2 The galaxy environment

The MUSE observations of this field presented in Section 2.4 have uncovered 129 objects in the MUSE field of view with pseudo *r*-band magnitude ranging from $AB(r) = 20.5$ to 27 mag in addition to the QSO. Of the 64 objects brighter than $AB(r) = 25$ mag, we are able to determine a robust redshift for 51, reaching a survey completeness of 80 per cent. The redshifts of spectroscopically identified galaxies in this field range from $z_{\rm gal} = 0.20$ to $z_{\rm gal} = 3.668$. Similar to the LLS towards J2308−5258 (see Section 4.3), only one galaxy is found in the vicinity of the LLS at line-of-sight velocity offset ${\rm d}v_{\rm gal} = +105$ km s^{-1} and angular distance $\theta = 11.9$ arcsec, corresponding to $d = 67$ pkpc at the redshift of the LLS (Fig. 10). Different from the configuration between the QSO probe and the LLS absorbing galaxy in J2308−5258, the QSO here probes the diffuse gas at ≈27°

Downloaded from https://academic.oup.com/mnras/article/497/1/498/5859973 by CNRS - ISTO user on 09 August 2022

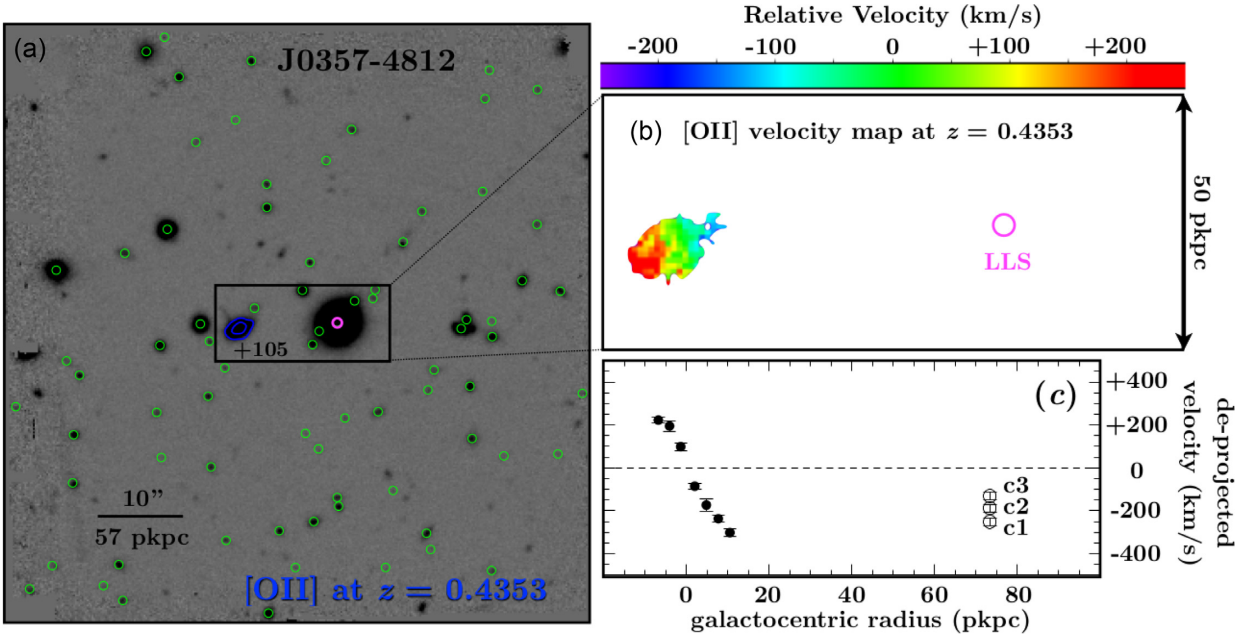

Figure 10. The galaxy environment uncovered by MUSE for the LLS at $z_{\rm abs} = 0.4353$ towards J0357−4812. The pseudo *r*-band image from Fig. 2 is reproduced in panel (*a*). North is up and east is to the left. Of the 77 spectroscopically identified galaxies in the MUSE field of view (green circles), only one galaxy (highlighted in blue contours) is found in the vicinity of the LLS at $\theta = 11.9$ arcsec (or $d = 67$ pkpc) and $\mathrm{d}v_{\rm gal} = +105$ km s^{-1}. The [O II] emission contours of constant surface brightness 0.25 and 1.25×10^{-17} erg s^{-1} cm^{-2} arcsec^{-2} are superimposed on top of the pseudo *r*-band image. The line-of-sight velocity map of [O II] emission is presented in panel (*b*) with zero velocity corresponding to $z_{\rm abs} = 0.4353$. The location of the LLS is marked by an open magenta circle. The absorbing galaxy displays a clear velocity gradient along the long axis, supporting the presence of a rotating disc. Panel (*c*) shows the de-projected rotation velocity along the disc plane as a function of galactocentric radius (solid points). Here, zero velocity is shifted from the LLS to the systemic redshift of the galaxy. For comparison, the three strongest H I absorbing components (c1, c2, and c3 from Table 6) of the LLS along the QSO sightline are also included in the plot, under the assumption that the gas is moving along the plane extended from the inclined optical disc. The de-projected velocities of the three components are consistent with a general rotation motion with the galaxy (see the text for further discussion).

from the major axis of the inclined disc (see below). The remaining spectroscopically identified galaxies in the MUSE field are all at a cosmologically distinct redshift with a velocity separation exceeding $|\mathrm{d}v_{\rm gal}| = 1000$ km s^{-1} from the LLS. The observed *r*-band magnitude of the LLS-absorbing galaxy is $AB(r) = 20.7$, while objects without a robust redshift measurement are all fainter than $AB(r) = 23.3$ mag. Any additional galaxy in the vicinity of the LLS will have to be more than 10 times fainter with intrinsic luminosity $< 0.14\,L_*$.

The optical spectrum of the absorbing galaxy at $d = 67$ pkpc is presented in Fig. 11, which is characterized by strong absorption features, together with weak [O II] and H β emission lines. In particular, it exhibits prominent Ca II absorption along with strong Balmer absorption lines. Details regarding the properties of this galaxy are presented in Appendix C. In summary, the galaxy is luminous with an unobscured SFR of $\approx 0.28\,\mathrm{M}_\odot\,\mathrm{yr}^{-1}$ based on the total integrated [O II] line flux and the star formation calibrator of Kewley et al. (2004). The observed *r*-band magnitude, $AB(r) = 20.7$, and rest-frame $g-r$ colour translate to an intrinsic *r*-band absolute magnitude of $M_r = -21.7$ (corresponding to $1.4\,L_*$) based on an early-type disc galaxy template and an underlying stellar mass of $\log M_{\rm star}/\mathrm{M}_\odot = 10.4$. The observed and derived properties of the galaxy are presented in columns (2) through (11) of Table 7.

The line-of-sight velocity map presented in panel (*b*) of Fig. 10 shows that the absorbing galaxy displays a clear velocity gradient along the long axis, from $\approx +250$ km s^{-1} on the south-east (lower-left) side to ≈ -110 km s^{-1} on the north-west (upper-right) side of the galaxy with the zero velocity corresponding to the systemic redshift, $z = 0.4353$, of the strongest component (c2 in Table 6) in the LLS at $d = 67$ pkpc to the west. The de-projected rotation

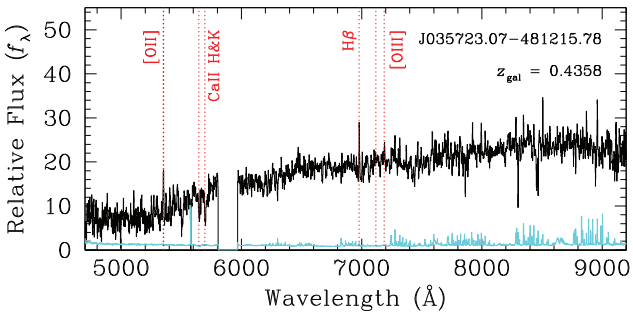

Figure 11. Optical spectrum of the galaxy identified in the vicinity of the LLS at $z_{\rm abs} = 0.4353$ towards J0357−4812 from MUSE observations. The corresponding 1σ error spectrum is shown in cyan. The galaxy is bright and the spectrum exhibits prominent absorption features along with weak [O II] and H β emission lines (highlighted in red dotted lines with corresponding line identifications). In addition to the Ca II absorption doublet, the spectrum also exhibits strong Balmer absorption lines, indicating the presence of mixed stellar populations.

velocity along the disc plane as a function of galactocentric radius is presented in panel (*c*) of Fig. 10 (solid points) with zero velocity corresponding to the systemic redshift of the galaxy (see Appendix C for details). Adopting $\mathrm{d}v_{\rm deproj} \approx +225$ km s^{-1} to be the maximum rotation velocity would imply an underlying dark matter halo mass of $M_h \approx 10^{12}\,\mathrm{M}_\odot$ and a stellar mass to dark matter halo mass ratio of $M_{\rm star}/M_h \approx 2.5$ per cent. The three H I absorbing components containing >99 per cent of the total N(H I) (c1, c2, and c3 from Table 6) of the LLS are found to be moving along the same direction

Downloaded from https://academic.oup.com/mnras/article/497/1/498/5859973 by CNRS - ISTO user on 09 August 2022

as the optical disc at a velocity, ranging from $dv_{\rm deproj}({\rm LLS}) = -130$ to -250 km s^{-1} (open circles in panel *c* of Fig. 10). The observed co-rotation between the gas and the galaxy suggests that the LLS originates in a rotating halo or an extended disc plane (e.g. Steidel et al. 2002; Chen et al. 2005; Diamond-Stanic et al. 2016; Martin et al. 2019) with contributions from either extraplanar gas and/or high-velocity clouds (e.g. Heald et al. 2011). Interestingly, component 3 with the largest N(Mg II) (and likely higher gas metallicity; see discussion in Section 5.2) also exhibits the largest lag in $|dv_{\rm deproj}|$ (see Fig. 4).

5 DISCUSSION

The LLS survey in the CUBS QSO sample has uncovered five new LLSs with $\tau_{912} \gtrsim 1$ at $z_{\rm abs} = 0.3640-0.6226$ and five pLLS with $\tau_{912} = 0.2-1$ at $z_{\rm abs} = 0.2603-0.9372$. While the number of newly identified LLSs is small, these represent a uniform and unbiased sample of optically thick absorbers identified along random QSO sightlines with log N(H I)/cm$^{-2} \gtrsim 16.5$. Common features of the newly identified LLSs include: (1) multicomponent kinematic profiles, indicating a clumpy medium and (2) a simultaneous presence of ionic species in multiple ionization states, suggesting a multiphase nature of the gas. These features have important implications for studying the ionization state and metallicity of the gas.

Deep galaxy survey data in the LLS fields have revealed a diverse range of galaxy environments around these optically thick absorbers, from a massive quiescent halo, a low-mass dwarf galaxy pair, a co-rotating gaseous halo/disc, to possibly intragroup medium of a galaxy group. A joint analysis, combining absorption-line studies of newly discovered LLSs and the associated galaxy survey data from the CUBS program, has offered important new insights into the connection between optically thick gas and galaxies, as well as the physical origin of metal-line absorbers. In this section, we discuss the implications of our sample for the incidence of LLSs at $z < 1$ and the physical properties of these absorbers, and the galactic environment uncovered from our galaxy survey.

5.1 Incidence of Lyman limit systems at $z < 1$

Because of their optically thick nature, the rate of incidence of LLSs is an important quantity for constraining the mean free path of ionizing photons and for computing the IGM photoionization rate. It also places constraints on the covering fraction of optically thick gas connected to infalling clouds and/or outflows in galaxy haloes (e.g. Hafen et al. 2017). Previous surveys have yielded a number density of LLSs per unit redshift per sightline in the range of $n(z) \approx 0.3-0.7$ at $z < 1$ (e.g. Songaila & Cowie 2010, for a compilation of early results with updates from Ribaudo et al. 2011; Shull et al. 2017). The large uncertainty underscores the challenge in conducting LLS surveys. First, surveys for LLSs at low redshifts rely on UV spectroscopy from space and therefore require a sample of UV-bright QSOs at $z_{\rm QSO} \gtrsim 1$ as the background probes. Secondly, these systems are rare and when an LLS occurs, it also attenuates the background QSO light and further reduces the survey path and sensitivity for uncovering additional Lyman limit features at lower redshift. This is seen in two of the CUBS QSO sightlines in Table 5, J0111−0316 and J2135−5316, which exhibit the two strongest LLSs found in our survey and consequently $\Delta z_{\rm LL}$ is substantially reduced for those two sightlines.

The consequence of attenuated background QSO light when an LLS occurs has important implications for the sample definition of QSOs employed for an unbiased CGM survey. UV-bright QSOs are biased against finding LLSs which, when unaccounted for, would lead to an underestimate of the incidence of these optically thick systems (e.g. Tytler 1982). Previous LLS surveys relying on archival sightlines to maximize the redshift survey path-length for these relatively rare systems have attempted to minimize such a bias by excluding QSO sightlines that are known to be biased against LLSs (e.g. Ribaudo et al. 2011). However, the sample is inherently heterogeneous and likely contains implicit bias. A recent study of the *GALEX* FUV–NUV colours of a sample of over 9000 NUV-selected QSOs (see the illustration in the top panel of Fig. 1) indeed suggests that the number density of LLSs at $z < 1$ may have been underestimated (Deharveng et al. 2019).

The CUBS QSO sample is selected to be at $z_{\rm QSO} \approx 0.8$–1.4 and bright in the *GALEX* NUV channel (1770–2730 Å). As outlined in Section 2, these selection criteria are motivated by a key scientific goal of studying the inner CGM ($d \lesssim 100$ pkpc) at $z \lesssim 1$ where a high incidence of optically thick absorbers is expected. The QSO sample is therefore also optimized for an unbiased search of LLS at $z < 1$. The summary in Table 5 shows that the entire CUBS QSO sample offers a total survey path-length of $\Delta z_{\rm LL} = 9.31$ for LLSs at $z = 0.21$–0.94. To estimate the number density of low-redshift LLSs and the associated uncertainties, we perform a bootstrap resampling routine. Specifically, we randomly resample the parent CUBS QSO sightlines with replacement to generate a new QSO sample containing the same number of QSOs. For each Lyman limit decrement in the new QSO sample, a new τ_{912} is generated from randomly sampling the Gaussian error around the measured τ_{912} reported in Table 5. This exercise is repeated 1000 times to produce a distribution of newly estimated number density $n(z)$ of the LLSs. The resulting 16 and 84 percentiles mark the 68 per cent confidence interval of the best estimated $n(z)$.

Our survey yields a number density estimate of $n(z) = 0.43^{+0.26}_{-0.18}$ for systems with $\tau_{912} > 1$. This is consistent with expectations from previous archival studies by Ribaudo et al. (2011) and Shull et al. (2017). It is, however, evident from Table 5 that most of the newly discovered LLSs in the CUBS QSO sample exhibit τ_{912} significantly greater than one. We repeat the number density measurement for two different thresholds with $\tau_{912} > 2$ and $\tau_{912} > 0.2$. The results are presented in Fig. 12, along with measurements from previous archival studies for comparison. For $\tau_{912} > 2$, we find $n(z) = 0.43^{+0.24}_{-0.21}$ in comparison to $n(z) = 0.37 \pm 0.10$ from Ribaudo et al. (2011). For $\tau_{912} > 0.2$, we find $n(z) = 1.08^{+0.31}_{-0.25}$ in comparison to $n(z) = 0.73^{+0.23}_{-0.18}$ from Shull et al. (2017). Our best estimated $n(z)$ for these strong H I absorbers are higher than previously reported values, but the uncertainties are large due to the small QSO sample.

5.2 The origin of Lyman limit systems

We have shown in Section 3.2 that in order to fully characterize the Lyman series associated with each LLS, it is necessary to incorporate a multicomponent structure for the absorber. Specifically, while the strongest component explains the highest order Lyman series lines all the way to the Lyman discontinuity, additional components are needed to explain the first few Lyman lines with the largest oscillator strengths (see also Chen et al. 2018; Zahedy et al. 2019). This multicomponent structure is also supported by the associated ionic transitions. In particular, nearly all H I components of log N(H I)/cm$^{-2} > 16.8$ exhibit associated Mg II components that are fully resolved in the ground-based optical Echelle spectra (Fig. 4). While COS does not fully resolve the component structure of additional FUV lines such as C II, C III, N II, and Si II, there is a broad agreement in the overall line shape (including both line width

Downloaded from https://academic.oup.com/mnras/article/497/1/498/5859973 by CNRS - ISTO user on 09 August 2022

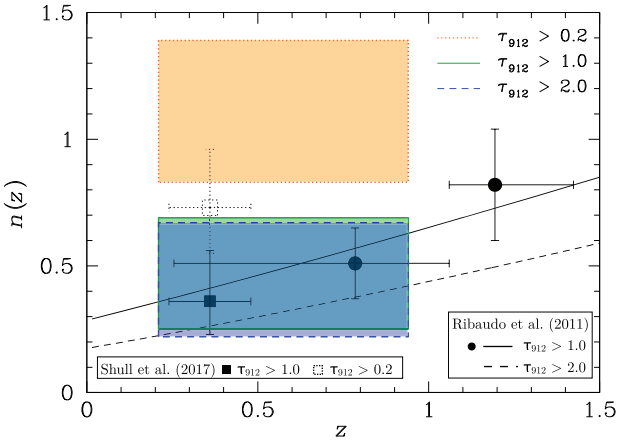

Figure 12. The rate of incidence of optically thick H I absorbers at $z \lesssim 1$ from the CUBS QSO sample. The measurements are made for three different τ_{912} thresholds, from $\tau_{912} > 2$ (blue, dashed rectangle), $\tau_{912} > 1$ (green, solid rectangle), to $\tau_{912} > 0.2$ (orange, dotted rectangle). The height of each rectangle represents the 68 per cent confidence interval estimated from a bootstrap resampling exercise described in the text, and the width represents the redshift interval surveyed. Previous measurements and associated 1σ uncertainties from Ribaudo et al. (2011) are shown in solid points, along with their best-fitting redshift evolution models for $\tau_{912} > 1$ (solid curve) and for $\tau_{912} > 2$ (dashed curve). The measurements and 1σ errors from Shull et al. (2017) are shown in squares.

and centroid) of these FUV transitions with the relative component strength displayed in the resolved Mg II components. The agreement in the absorption profiles between low- and intermediate-ionization transitions supports a scenario that these ions are linked kinematically and share a common velocity field.

We also note that O VI absorption is observed in all but the DLA at $z_{\rm abs} = 0.5762$ towards J0111−0316. Three of the four O VI-bearing LLSs, towards J0248−4048, J0357−4812, and J2308−5258, display a broad and relatively shallow O VI absorption profile. While the component structures of the O VI lines are not resolved, their kinematic profiles share a similar asymmetry with the associated C III absorption line. Such agreement suggests a multiphase nature of these LLSs (see also, Zahedy et al. 2019). A notable exception is the LLS at $z_{\rm abs} = 0.6226$ towards J2135−5316, which displays a single strong O VI component at $dv_c = -120$ km s^{-1} with corresponding C III and a relatively weak H I component of log N_c(H I)/cm^{-2} = 15.4 and $b_c \approx 27$ km s^{-1}, but no other low-ionization transitions. The co-presence of C III and O VI with consistent kinematic profiles with H I suggests that the gas is predominantly photoionized (e.g. Thom & Chen 2008; Tripp et al. 2008; Stern et al. 2018). However, the absence of O VI around dominant H I components at $|dv_c| < 100$ km s^{-1} is in stark contrast to the other three LLSs towards J0248−4048, J0357−4812, and J2308−5258.

Comparisons of heavy ions to neutral hydrogen column density ratios between individual components have also revealed a chemical inhomogeneity within a single LLS. Fig. 13 shows the observed N(Mg II)/N(H I) ratios both for individual components (pentagons) and for each LLS as a whole (horizontal bars). Only components with log N(H I)/cm^{-2} > 15 are included, because the sensitivity limit for N(Mg II) allowed by the optical Echelle spectra become unconstraining for weaker H I components. In at least three of the five new LLSs in the CUBS sample, large differential N(Mg II)/N(H I) is directly seen between different components. For example, the strongest Mg II component of the LLS at $z_{\rm abs} = 0.4353$ towards J0357−4812 (c3 in Table 6) occurs at $dv_c = +31.4$ km s^{-1} and contains 10 times less H I than the strongest H I component (c2 in Table 6) at $dv_c = 0$ km s^{-1}. Consequently, the two components exhibit N(Mg II)/N(H I) ratios that differ by more than a factor of 10 (panel *e* of Fig. 13).

Although inferring gas metallicity from the observed N(Mg II)/N(H I) requires knowledge of the ionization state of the gas (which is presented in a separate paper by Zahedy et al., in preparation), we note that under photoionization equilibrium the observed differences in N_c(Mg II)/N_c(H I) could serve as a rough guide for inferring the underlying gas metallicities for a limited gas density range under photoionization equilibrium. This is understood based on the expectation that the abundance ratio of total Mg/H is related to N(Mg II)/N(H I) according to (Mg/H) × ($f_{\rm Mg^+}$/ $f_{\rm H^0}$) = Mg$^+$/H^0. For a typical gas density of diffuse halo gas in the range $n_{\rm H} \approx 0.01$–0.001 cm^{-3} (corresponding to an ionization parameter in the range of log $U \approx -3$ to −2 at $z < 1$, assuming ionization equilibrium and no dust depletion), the ratio of ion fractions, $f_{\rm Mg^+}$/ $f_{\rm H^0}$, does not change by more than a factor of two (e.g. Chen & Tinker 2008; Wotta et al. 2016). The large variation by more than a factor of 10 in the observed N(Mg II)/N(H I) between individual components therefore suggests large differential chemical enrichment levels in individual LLSs (see also Prochter et al. 2010; Zahedy et al. 2019).

In summary, newly uncovered LLSs in the CUBS QSO sample exhibit a multicomponent absorption structure with differential chemical enrichment levels as well as ionization states. The gas is complex in terms of its kinematics and ionization state, and inhomogeneous in chemical enrichment. These properties have important implications both for the physical origins of these optically thick absorbers and for ionization and metallicity measurements that are based on integrated column density ratios over all components. They also underscore the scientific value of high-resolution absorption spectra in resolving the clumpy, multiphase gas (e.g. Rudie et al. 2019; Zahedy et al. 2019).

5.3 Galaxy environment of Lyman limit systems

In addition to complex gas kinematics, ionization states, and chemical enrichment histories of the gas revealed in the QSO absorption spectra, the accompanying galaxy survey has also revealed a diverse range of galaxy environments around the new LLSs in the CUBS sample. To summarize the galaxy environment of the LLSs, we show in the top panels of Fig. 13 the stellar mass versus velocity distribution of galaxies identified at $d < 300$ pkpc and $|dv_{\rm gal}| < 300$ km s^{-1} from the LLS. In addition, we present the $M_{\rm star}$ versus d distribution in Fig. 14. It shows the properties of galaxies identified at $d <$ 300 pkpc of the LLSs broadly classified into three different spectral types: evolved galaxies with an absorption-line dominated spectrum (circles), intermediate galaxies displaying both nebular emission and stellar absorption features (triangles), and star-forming galaxies displaying predominantly nebular emission lines (squares). As described in Section 4, the MUSE data enable a highly complete galaxy survey to faint magnitudes, reaching 100 per cent completeness at $AB(r) \leq 23$ mag and $\gtrsim 75$ per cent at $AB(r) \leq 25$ mag, in the field of view that corresponds roughly to an area of ≈300 pkpc in radius at the redshifts of these absorbers. The absence of additional galaxies in the vicinities of the two LLSs towards J2308−5258 (panel *c*) and J0357−4812 (panel *e*) is therefore particularly interesting. At the redshifts of these two LLSs, our galaxy survey completeness ensures that any additional galaxy in the vicinity of the LLS would be faint with intrinsic luminosity $\lesssim 0.1\ L_*$. It indicates that the LLSs and the associated absorbing galaxies (both super-L_* and massive) reside in a relatively isolated environment. Galaxies identified at $d < 300$ pkpc

Downloaded from https://academic.oup.com/mnras/article/497/1/498/5859973 by CNRS - ISTO user on 09 August 2022

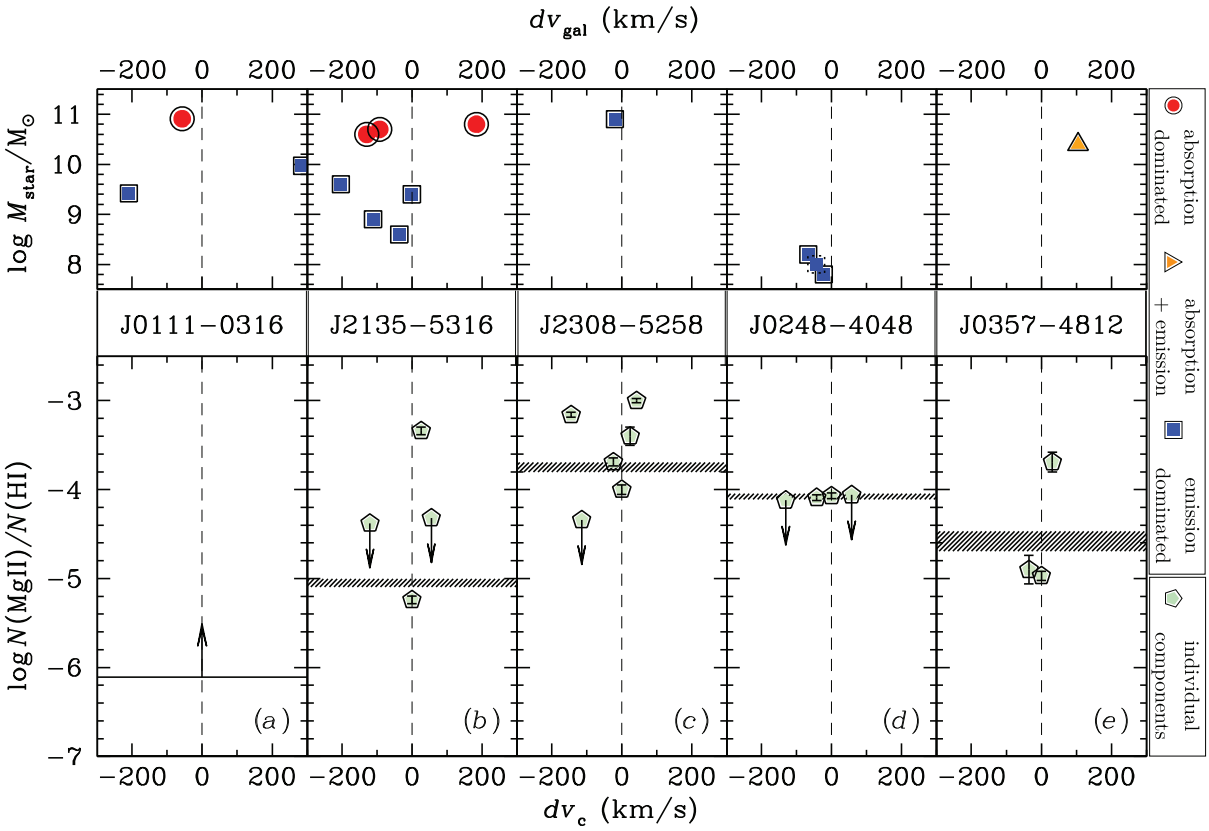

Figure 13. *Top*: Stellar mass versus velocity distribution of galaxies identified at $d < 300$ pkpc and $|\mathrm{d}v_{\mathrm{gal}}| < 300$ km s^{-1} from the LLS (see Table 7). Blue squares represent emission-line dominated star-forming galaxies; red circles represent absorption-line (such as Ca II H&K) dominated galaxies; and orange triangles represent galaxies displaying both emission and absorption in their optical spectra. The square with a dotted outline represents the galaxy at $d =$ 15 pkpc towards J0248−4048, because its mass is inferred from the estimated gas-phase metallicity and the mass–metallicity relation of Berg et al. (2012). *Bottom*: Observed N(Mg II)/N(H I) ratios of five new LLSs from the CUBS sample versus the line-of-sight velocity offset from the strongest H I component ($\mathrm{d}v_c$ from Table 6). The fields are ordered with decreasing N(H I) from left to right. Pentagons are for individual components of log N(H I)/cm^{-2} > 15, while the horizontal bar in each panel represents the integrated column density ratio and its associated uncertainty over all components for each LLS. Large scatter between individual components is present in three of the four strong H I absorbers for which the component structure is resolved for both Mg II and H I (panels *b*, *c*, and *e*), and absorbing gas with high N(Mg II)/N(H I) would be missed in integrated column density ratios.

of the H_2-bearing DLA are included for comparison. As described in Boettcher et al. (in preparation), six additional galaxies are found at $|\mathrm{d}v_c| < 300$ km s^{-1} at $d = 300-600$ pkpc from the ongoing deep- and wide-field galaxy survey on the Magellan Telescopes. However, within the loose group of nine galaxies, the evolved galaxy at $d = 42$ pkpc is the most massive member, contributing ≈40 per cent of the total stellar mass of the group.

Similarly, the LLS at $z_{\mathrm{abs}} = 0.6226$ towards J2135−5316 is found associated with a massive galaxy group of dynamical mass $M_{\mathrm{dyn}} \approx 1.1 \times 10^{13}$ M$_\odot$ (comparable in mass to haloes hosting luminous red galaxies; Padmanabhan et al. 2007) at $d_{\mathrm{group}} = 177$ pkpc. The massive group environment provides a potential physical explanation for the lack of O VI surrounding the strong H I components (see Fig. 4). Because the gas temperature in a massive group is expected to be high, $T \sim 6 \times 10^6$ K, heavy elements, including oxygen, are expected to be ionized to higher states (e.g. Oppenheimer et al. 2016). Indeed, Wijers, Schaye & Oppenheimer (2020) predict covering fractions of only ≈25 per cent for O VI gas of log N(O VI)/cm^{-2} > 13.5 at $d \approx 200$ pkpc from a galaxy with log M_{star}/M$_\odot$ > 11. At the same time, the likely photoionized O VI component at $\mathrm{d}v_c = -120$ km s^{-1} with log N(H I)/cm^{-2} = 15.4 may be attributed to halo clouds associated with the nearby low-mass satellite of log M_{star}/M$_\odot$ = 8.9 at $d = 72$ pkpc and $\Delta v = -111$ km s^{-1}. However, the dominant H I component of this LLS contains the second highest N(H I) uncovered in our survey with log N(H I)/cm^{-2} = 18 and only relatively weak Mg II absorption. The low N(Mg II)/N(H I) ratio (panel *b* of Fig. 13) implies a relatively low gas metallicity. It is therefore likely that the LLS originate in dense gaseous streams accreted from the IGM (e.g. Hafen et al. 2017).

In contrast to the two strongest H I absorbers uncovered in our survey, the LLS at $z_{\mathrm{abs}} = 0.3640$ towards J0248−4048 is found to be associated with a pair of low-mass dwarfs of ≈0.01–0.03 L_* (log M_{star}/M$_\odot$ ≈ 8) and ISM metallicity of ≈10 per cent solar at $d = 15$ and 37 pkpc. The galaxy at $d = 15$ pkpc is the closest absorbing galaxy uncovered in our survey. However, the total H I column density is merely log N(H I)/cm^{-2} = 17.6. This low N(H I) at a small distance from a low-mass dwarf is similar to what is observed in local dwarf irregular galaxies (e.g. Hunter et al. 2012; Johnson et al. 2017). The low-mass nature (and presumably shallow gravitational potential well) in the presence of the UV background makes it difficult to maintain a large amount of neutral gas (e.g. Johnson et al. 2017). The two dominant H I components at $\mathrm{d}v_c = -42$ and $\mathrm{d}v_c = 0$ km s^{-1} (c2 and c3) of this LLS exhibit comparably modest N_c(Mg II)/N_c(H I) ratios (panel *d* of Fig. 13), suggesting a chemical enrichment level comparable to the 10 per cent solar metallicity (e.g. Wotta et al. 2016) inferred for the ISM of the two star-

Downloaded from https://academic.oup.com/mnras/article/497/1/498/5859973 by CNRS - ISTO user on 09 August 2022

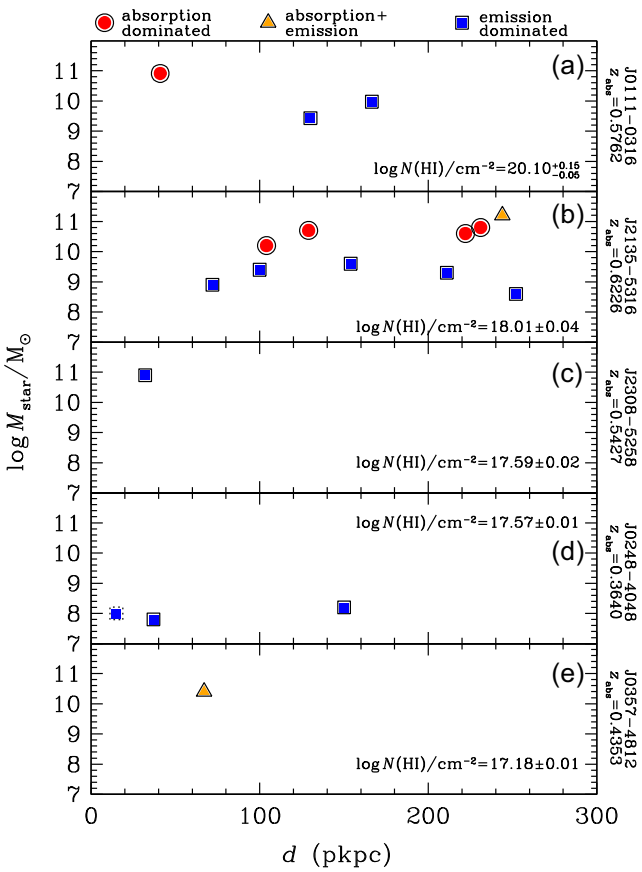

Figure 14. Summary of the galaxy environment uncovered from follow-up deep galaxy surveys of the five new optically thick absorbers in the CUBS sample. The panels display $M_{\rm star}$ versus d for galaxies found in the vicinities of the LLSs along the sightlines towards J0111−0316 (panel *a*; from Boettcher et al., in preparation), J2135−5316 (panel *b*), J2308−5258 (panel *c*), J0248−4048 (panel *d*), and J0357−4812 (panel *e*). The fields are ordered with decreasing N(H I) from top to down. Blue squares represent emission-line dominated star-forming galaxies; red circles represent absorption-line (such as Ca II H&K) dominated galaxies; and orange triangles represent galaxies displaying both emission and absorption in their optical spectra. The galaxy at $d = 15$ pkpc towards J0248−4048 is included for comparison (shown in dotted outline in panel *d*), but note that, as discussed in Section 4.4, the mass is inferred from the estimated gas-phase metallicity and the mass–metallicity relation of Berg et al. (2012). MUSE data enable a galaxy survey to faint magnitudes, reaching 100 per cent completeness at $AB(r) \leq 23$ mag and $\gtrsim$ 75 per cent at $AB(r) \leq 25$ mag, in the field of view that corresponds roughly to an area of ≈300 pkpc in radius at the redshifts of these absorbers. The absence of additional galaxies in the vicinities of the two LLSs towards J0357−4812 and J2308−5258 therefore indicates that the LLSs and the associated galaxies (both are super-L_*) reside in a relatively isolated environment.

forming dwarfs. If confirmed by a more detailed ionization analysis, the optically thick gas most likely originates in expelled ISM gas from the nearby dwarf galaxies, either through galaxy interactions or starburst driven outflows.

Both the LLSs towards J0357−4812 and J2308−5258 are found in a relatively isolated environment with only one luminous, star-forming galaxy found at $d < 300$ pkpc and $|{\rm d}v_{\rm gal}| < 300$ km s^{-1}. Incorporating results from ongoing deep- and wide-field galaxy survey will provide a more complete view of the larger scale galaxy environment. In the immediate vicinity of the LLS, however, the LLS at $z_{\rm abs} = 0.4353$ towards J0357−4812 is found to be associated with a luminous galaxy of $\approx 1.4\,L_*$ at $d = 67$ pkpc with the QSO sightline intercepting the diffuse halo at ≈27° from the major axis (see Section 4.5). The relative velocity offsets of the absorbing components are consistent with the gas co-rotating with the disc, with the high-metallicity component (c3) showing the largest "lag" in velocity. If the low-metallicity components (c1 and c2) originate in accreted gaseous streams that co-rotate, possible origins for the high-metallicity component (c3) include fountain flows, extraplanar gas, or disrupted satellites (see Heald et al. 2011 and Putman, Peek & Joung 2012, for a review).

In contrast, the LLS at $z_{\rm abs} = 0.5427$ towards J2308−5258 is found to be associated with a luminous, star-forming galaxy of $\approx 2\,L_*$ at $d = 32$ pkpc with the QSO sightline intercepting the diffuse halo at ≈28° from the minor axis (see Section 4.3). The Mg II absorption profile is resolved into five separate components with four satellite components at $|{\rm d}v_c| > 0$ (c1, c3, c5, and c6) sharing comparable absorption strength, while the corresponding N(H I) differ by a factor of ≈ 6. Following the same argument described above, the different N_c(Mg II)/N_c(H I) ratios suggest that the two outlying components at ${\rm d}v_c = -144$ and +42 km s^{-1}, c1 and c6, respectively, contain the highest metallicity gas in this LLS (panel *c* in Fig. 13). The combination of a close proximity to a star-forming galaxy and a geometric alignment of the QSO sightline near the minor axis of the galaxy makes starburst outflows an attractive scenario for the LLS (e.g. Heckman, Armus & Miley 1990; Shen et al. 2013). However, the large scatter in gas metallicity inferred from N_c(Mg II)/N_c(H I) between different components also suggests that additional sources are needed to fully explain all the components seen in the LLS, particularly the central component (c4) that dominates the total N(H I) (e.g. Hafen et al. 2019).

In summary, our galaxy survey is sensitive for detecting galaxies fainter than 0.1 L_* at $d \lesssim 300$ kpc from the LLSs. A diverse range of galaxy properties is seen around these optically thick absorbers, from a low-mass dwarf galaxy pair, a co-rotating gaseous halo/disc, a star-forming galaxy, a massive quiescent halo, to a galaxy group. The closest galaxies found for the LLSs have projected distance ranging from $d = 16$ pkpc to $d = 72$ pkpc and intrinsic luminosity from $\approx 0.01\,L_*$ (or log $M_{\rm star}/{\rm M}_\odot = 7.8$) to $\approx 3\,L_*$ (or log $M_{\rm star}/{\rm M}_\odot = 10.9$). This wide range of galaxy properties uncovered for the sample of five LLSs encompasses what is seen previously for individual systems at $z_{\rm abs} < 1$ (e.g. Kacprzak et al. 2010; Neeleman et al. 2016; Péroux et al. 2017; Chen et al. 2019a), highlighting the complex origins of these absorbers.

While no clear correlation is seen between the observed over-density of galaxies and the kinematic spread of low-ionization species, the observed absorption strengths of low-ionization transitions appear to correlate with the projected distance of the closest galaxy found. Specifically, both LLSs with weak Mg II features of log N(Mg II)/cm^{-2} < 13 (along the sightlines towards J2135−5316 and J0357−4812) have the closest galaxy found at $d > 60$ pkpc, whereas the remaining three have log N(Mg II)/cm^{-2} > 13.4 and a galaxy found at $d < 50$ pkpc. The observed trend is consistent with previous findings that the distance to a galaxy is a more dominant factor than the mass of the galaxies in driving the observed Mg II absorption strength (e.g. Chen et al. 2010a, b).

6 SUMMARY AND CONCLUSIONS

We present initial results from the CUBS program, designed to map diffuse baryonic structures at $z \lesssim 1$, using absorption-line spectroscopy of 15 UV bright QSOs with matching deep galaxy survey data. CUBS QSOs are selected based on their NUV brightness to avoid biases against LLSs at $z_{\rm abs} < 1$, which are expected to attenuate the background QSO light in the FUV spectral window.

Downloaded from https://academic.oup.com/mnras/article/497/1/498/5859973 by CNRS - ISTO user on 09 August 2022

Combining high-quality *HST* COS FUV absorption spectra with optical Echelle spectra of the QSOs and deep galaxy survey data of the QSO fields obtained from the ground, we carry out a joint study of LLSs and their associated galaxies to gain insight into the connection between optically thick gas and galaxies, as well as the physical origin of metal-line absorbers. Our findings are summarized below:

(1) The COS spectra of the 15 NUV bright QSOs in the CUBS sample provide a total redshift survey path-length of $\Delta z_{\rm LL} = 9.3$ for searching for LLSs. We report five new LLSs of $\log N({\rm H\,I})/{\rm cm}^{-2} \gtrsim 17.2$ and five new pLLS of $\log N({\rm H\,I})/{\rm cm}^{-2} = 16.5 - 17.2$, leading to a number density of $n(z) = 0.43^{+0.26}_{-0.18}$ for LLS and $n(z) = 1.08^{+0.31}_{-0.25}$ for pLLS and LLS combined at $z_{\rm abs} < 1$. While the uncertainties are large due to the small QSO sample, there is a tantalizing indication that previously reported $n(z)$ of these strong H I absorbers may have been underestimated, possibly due to FUV selection bias.

(2) All newly uncovered LLSs exhibit a multicomponent structure and associated heavy ions from low-, intermediate-, to high-ionization states. There is broad agreement in the overall line profiles of both low- and intermediate-ionization species, indicating that different ionic species are linked kinematically and share a common velocity field. At the same time, O VI is detected in all but the DLA at $z_{\rm abs} = 0.5762$ towards J0111−0316. Three of the four O VI-bearing optically thick absorbers display a broad and relatively shallow absorption profile that traces the broad kinematic properties of associated low- and intermediate-ionization species, while the 4th LLS displays only a single strong O VI in one H I component that contains ≈0.2 per cent of the total N(H I).

(3) Large differential $N({\rm Mg\,II})/N({\rm H\,I})$ ratios, by more than a factor of 10, are directly seen across different components of individual LLSs, suggesting inhomogeneous chemical enrichment as well as ionization state in individual galaxy haloes. A detailed ionization analysis presented in Zahedy et al. (in preparation) will quantify the extent of density and metallicity fluctuations in individual systems. Here, we show that high $N({\rm Mg\,II})/N({\rm H\,I})$ components would be missed in integrated column density calculations, which underscores the scientific value of high-resolution absorption spectra in resolving the clumpy, multiphase gas.

(4) MUSE integral field spectroscopic data, covering a 1 arcmin × 1 arcmin field of view, has provided an ultradeep view of the environment around three of the five new LLSs. The galaxy survey in each field is 100 per cent complete to $AB(r) = 23$ mag (corresponding to $0.3\,L_*$ or fainter at the redshifts of the LLSs), and between 75 per cent and 90 per cent complete to $AB(r) = 25$ mag. A diverse range of galaxy environments is seen around these LLSs, from a massive quiescent halo, a low-mass dwarf galaxy pair, a co-rotating gaseous halo/disc, to a massive galaxy group. The closest galaxies found for the LLSs have projected distance ranging from $d = 16$ to $d = 72$ pkpc and intrinsic luminosity from $\approx 0.01\,L_*$ to $\approx 3\,L_*$. The wide range of galaxy environments further underscores the complexity in connecting gas to galaxies and the need for deep galaxy survey data to fully understand the origin of absorption-line systems.

In conclusion, we are constructing a legacy data set through the CUBS program to enable comprehensive studies of the co-evolution of galaxies and their surrounding gas at $z \lesssim 1$. While the combined space-based UV and ground-based optical Echelle absorption spectroscopy of distant QSOs provides a powerful tool for resolving the ionization states and chemical enrichment histories of the diffuse CGM/IGM over a broad range in gas density along 15 independent sightlines, the accompanying deep and wide galaxy survey data provide a sensitive record of the galaxy environment on both large and small scales. In addition to detailed ionization analyses of individual high-N(H I) absorbers presented in Boettcher et al. (in preparation), Cooper et al. (in preparation), Johnson et al. (in preparation), and Zahedy et al. (in preparation), in future papers we will probe the physical conditions, chemical composition, and kinematics of halo gas (at $d \lesssim 300$ pkpc) around galaxies with diverse star formation histories and examine the physical origin of different absorption-line systems based on their large-scale (≈1–10 pMpc) clustering amplitudes with known galaxies. Together with published samples at low and high redshift, we will also quantify the evolution of the CGM across 10 Gyr of cosmic evolution, with the CUBS data charting the critical period when the star formation history of the universe underwent its precipitous decline.

ACKNOWLEDGEMENTS

We thank an anonymous referee for timely and constructive comments that helped improve the presentation of the paper. We thank Ruari Mackenzie for prompt and helpful advice and guidance on MUSE data reduction, and Matteo Fossati for sharing the KUBEVIZ code and assistance on analysing the MUSE data cubes. We thank Dan Kelson for his expert assistance on reducing the galaxy survey data from the Magellan Telescopes. HWC, EB, and MCC acknowledge partial support from HST-GO-15163.001A and NSF AST-1715692 grants. TC and GCR acknowledge support from HST-GO-15163.015A. SC gratefully acknowledges support from Swiss National Science Foundation grant PP00P2_163824. SDJ acknowledges support from a NASA Hubble Fellowship (*HST*-HF2-51375.001-A). KLC acknowledges partial support from NSF AST-1615296. CAFG was supported by NSF through grants AST-1517491, AST-1715216, and CAREER award AST-1652522, by NASA through grant 17-ATP17-0067, by STScI through grants *HST*-GO-14681.011, *HST*-GO-14268.022-A, and *HST*-AR-14293.001-A, and by a Cottrell Scholar Award from the Research Corporation for Science Advancement. SL was funded by project FONDECYT 1191232. This work is based on observations made with ESO Telescopes at the Paranal Observatory under programme ID 0104.A-0147(A), observations made with the 6.5m Magellan Telescopes located at Las Campanas Observatory, and spectroscopic data gathered under the *HST*-GO-15163.01A program using the NASA/ESA *Hubble Space Telescope* operated by the Space Telescope Science Institute and the Association of Universities for Research in Astronomy, Inc., under NASA contract NAS 5-26555. This research has made use of NASA's Astrophysics Data System and the NASA/IPAC Extragalactic Database (NED) which is operated by the Jet Propulsion Laboratory, California Institute of Technology, under contract with the National Aeronautics and Space Administration.

This study is based on data gathered with the 6.5m Magellan Telescopes located at Las Campanas Observatory, ESO Telescopes at the Paranal Observatory, and the NASA/ESA *Hubble Space Telescope* operated by the Space Telescope Science Institute and the Association of Universities for Research in Astronomy, Inc., under NASA contract NAS 5-26555.

DATA AVAILABILITY

The data underlying this article will be shared on reasonable request to the corresponding author.

REFERENCES

Afruni A., Fraternali F., Pezzulli G., 2019, A&A, 625, A11
Asplund M., Grevesse N., Sauval A. J., Scott P., 2009, ARA&A, 47, 481

Downloaded from https://academic.oup.com/mnras/article/497/1/498/5859973 by CNRS - ISTO user on 09 August 2022

Bacon R. et al., 2010, in McLean I. S., Ramsay S. K., Takami H., eds, Proc. SPIE Conf. Ser. Vol. 7735, Ground-based and Airborne Instrumentation for Astronomy III. SPIE, Bellingham, p. 773508
Baldwin J. A., Phillips M. M., Terlevich R., 1981, PASP, 93, 5
Berg D. A. et al., 2012, ApJ, 754, 98
Bernstein R., Shectman S. A., Gunnels S. M., Mochnacki S., Athey A. E., 2003, in Iye M., Moorwood A. F. M. , eds, Proc. SPIE Conf. Ser. Vol. 4841, Instrument Design and Performance for Optical/Infrared Ground-based Telescopes. SPIE, Bellingham, p. 1694
Bielby R., Crighton N. H. M., Fumagalli M., Morris S. L., Stott J. P., Tejos N., Cantalupo S., 2017, MNRAS, 468, 1373
Burchett J. N. et al., 2019, ApJ, 877, L20
Calzetti D., 1997, in Walle W. H., ed., AIP Conf. Ser. 408, The Ultraviolet Universe at Low and High Redshift. Am. Inst. Phys, New York, p. 403
Calzetti D., Armus L., Bohlin R. C., Kinney A. L., Koornneef J., Storchi-Bergmann T., 2000, ApJ, 533, 682
Cantalupo S. et al., 2019, MNRAS, 483, 5188
Chabrier G., 2003, PASP, 115, 763
Chen H.-W., 2017, in Knapen J. H., Lee J. C., Gil de Paz A., eds, Outskirts of Galaxies, Vol. 434. Astrophysics and Space Science Library, Springer, p. 291
Chen H.-W., Mulchaey J. S., 2009, ApJ, 701, 1219
Chen H.-W., Tinker J. L., 2008, ApJ, 687, 745
Chen H.-W., Lanzetta K. M., Webb J. K., Barcons X., 1998, ApJ, 498, 77
Chen H.-W., Lanzetta K. M., Webb J. K., Barcons X., 2001, ApJ, 559, 654
Chen H.-W., Kennicutt R. C., Jr, Rauch M., 2005, ApJ, 620, 703
Chen H.-W., Helsby J. E., Gauthier J.-R., Shectman S. A., Thompson I. B., Tinker J. L., 2010a, ApJ, 714, 1521
Chen H.-W., Wild V., Tinker J. L., Gauthier J.-R., Helsby J. E., Shectman S. A., Thompson I. B., 2010b, ApJ, 724, L176
Chen H.-W., Gauthier J.-R., Sharon K., Johnson S. D., Nair P., Liang C. J., 2014, MNRAS, 438, 1435
Chen H.-W., Zahedy F. S., Johnson S. D., Pierce R. M., Huang Y.-H., Weiner B. J., Gauthier J.-R., 2018, MNRAS, 479, 2547
Chen H.-W. et al., 2019a, MNRAS, 484, 431
Chen H.-W. et al., 2019b, ApJ, 878, L33
Cool R. J. et al., 2012, ApJ, 748, 10
Deharveng J.-M., Milliard B., Péroux C., Small T., 2019, A&A, 623, A149
Diamond-Stanic A. M., Coil A. L., Moustakas J., Tremonti C. A., Sell P. H., Mendez A. J., Hickox R. C., Rudnick G. H., 2016, ApJ, 824, 24
Dressler A., Hare T., Bigelow B. C., Osip D. J., 2006, in McLean I. S., Iye M., eds, Proc. SPIE Conf. Ser. Vol. 6269, Ground-based and Airborne Instrumentation for Astronomy. SPIE, Bellingham, p. 13
Drlica-Wagner A. et al., 2018, ApJS, 235, 33
Dubois Y., Peirani S., Pichon C., Devriendt J., Gavazzi R., Welker C., Volonteri M., 2016, MNRAS, 463, 3948
Eisenstein D. J. et al., 2011, AJ, 142, 72
Faucher-Giguère C.-A., 2020, MNRAS, 493, 1614
Faucher-Giguère C.-A., Kereš D., 2011, MNRAS, 412, L118
Faucher-Giguère C.-A., Hopkins P. F., Kereš D., Muratov A. L., Quataert E., Murray N., 2015, MNRAS, 449, 987
Faucher-Giguère C.-A., Feldmann R., Quataert E., Kereš D., Hopkins P. F., Murray N., 2016, MNRAS, 461, L32
Foreman-Mackey D., Hogg D. W., Lang D., Goodman J., 2013, PASP, 125, 306
Fossati M., Fumagalli M., Boselli A., Gavazzi G., Sun M., Wilman D. J., 2016, MNRAS, 455, 2028
French K. D., Yang Y., Zabludoff A., Narayanan D., Shirley Y., Walter F., Smith J.-D., Tremonti C. A., 2015, ApJ, 801, 1
Fumagalli M., Prochaska J. X., Kasen D., Dekel A., Ceverino D., Primack J. R., 2011, MNRAS, 418, 1796
Gordon K. D., Clayton G. C., Misselt K. A., Landolt A. U., Wolff M. J., 2003, ApJ, 594, 279
Green J. C. et al., 2012, ApJ, 744, 60
Hafen Z. et al., 2017, MNRAS, 469, 2292
Hafen Z. et al., 2019, MNRAS, 488, 1248
Heald G. et al., 2011, A&A, 526, A118
Heckman T. M., Armus L., Miley G. K., 1990, ApJS, 74, 833
Hewett P. C., Wild V., 2010, MNRAS, 405, 2302
Hopkins P. F., Kereš D., Oñorbe J., Faucher-Giguère C.-A., Quataert E., Murray N., Bullock J. S., 2014, MNRAS, 445, 581
Hummels C. B., Bryan G. L., Smith B. D., Turk M. J., 2013, MNRAS, 430, 1548
Hunter D. A. et al., 2012, AJ, 144, 134
Ji S. et al., 2019, MNRAS , in press
Johnson S. D., Chen H.-W., Mulchaey J. S., 2013, MNRAS, 434, 1765
Johnson S. D., Chen H.-W., Mulchaey J. S., 2015, MNRAS, 449, 3263
Johnson S. D., Chen H.-W. , Mulchaey J. S., Schaye J., Straka L. A., 2017, ApJ, 850, L10
Johnson S. D. et al., 2018, ApJ, 869, L1
Jones D. H. et al., 2009, MNRAS, 399, 683
Kacprzak G. G., 2017, in Fox A. J., Dave R., eds, Gas Accretion on to Galaxies, Vol. 430. Springer, p. 145
Kacprzak G. G., Murphy M. T., Churchill C. W., 2010, MNRAS, 406, 445
Kennicutt R. C., Jr, Evans N. J., 2012, ARA&A, 50, 531
Kewley L. J., Geller M. J., Jansen R. A., 2004, AJ, 127, 2002
Lamontagne R., Demers S., Wesemael F., Fontaine G., Irwin M. J., 2000, AJ, 119, 241
Lehner N., Wotta C. B., Howk J. C., O'Meara J. M., Oppenheimer B. D., Cooksey K. L., 2019, ApJ, 887, 5
Liang C. J., Kravtsov A. V., Agertz O., 2016, MNRAS, 458, 1164
Lofthouse E. K. et al., 2020, MNRAS, 491, 2057
Mackenzie R. et al., 2019, MNRAS, 487, 5070
Maller A. H., Bullock J. S., 2004, MNRAS, 355, 694
Marino R. A. et al., 2013, A&A, 559, A114
Martin C. L., Ho S. H., Kacprzak G. G., Churchill C. W., 2019, ApJ, 878, 84
Miller S. H., Ellis R. S., Newman A. B., Benson A., 2014, ApJ, 782, 115
Monroe T. R., Prochaska J. X., Tejos N., Worseck G., Hennawi J. F., Schmidt T., Tumlinson J., Shen Y., 2016, AJ, 152, 25
Muzahid S., Srianand R., Charlton J., 2015, MNRAS, 448, 2840
Muzahid S., Kacprzak G. G., Charlton J. C., Churchill C. W., 2016, ApJ, 823, 66
Naab T., Ostriker J. P., 2017, ARA&A, 55, 59
Neeleman M. et al., 2016, ApJ, 820, L39
Nelson D. et al., 2018, MNRAS, 477, 450
Oppenheimer B. D., Crain R. A., Schaye J., 2016, MNRAS, 460, 2157
Padmanabhan N. et al., 2007, MNRAS, 378, 852
Pascarelle S. M., Lanzetta K. M., Chen H.-W., Webb J. K., 2001, ApJ, 560, 101
Perlman E. S., Padovani P., Giommi P., Sambruna R., Jones L. R., Tzioumis A., Reynolds J., 1998, AJ, 115, 1253
Péroux C. et al., 2017, MNRAS, 464, 2053
Péroux C. et al., 2019, MNRAS, 485, 1595
Prochaska J. X. et al., 2017, ApJ, 837, 169
Prochter G. E., Prochaska J. X., O'Meara J. M., Burles C., Bernstein R. A., 2010, ApJ, 708, 169
Putman M. E., Peek J. E. G., Joung M. R., 2012, ARA&A, 50, 491
Qu Z., Bregman J. N., 2018, ApJ, 856, 5
Read J. I., Iorio G., Agertz O., Fraternali F., 2017, MNRAS, 467, 2019
Ribaudo J., Lehner N., Howk J. C., Werk J. K., Tripp T. M., Prochaska J. X., Meiring J. D., Tumlinson J., 2011, ApJ, 743, 207
Rowlands K., Wild V., Nesvadba N., Sibthorpe B., Mortier A., Lehnert M., da Cunha E., 2015, MNRAS, 448, 258
Rudie G. C. et al., 2012, ApJ, 750, 67
Rudie G. C., Steidel C. C., Shapley A. E., Pettini M., 2013, ApJ, 769, 146
Rudie G. C., Newman A. B., Murphy M. T., 2017, ApJ, 843, 98
Rudie G. C., Steidel C. C., Pettini M., Trainor R. F., Strom A. L., Hummels C. B., Reddy N. A., Shapley A. E., 2019, ApJ, 885, 61
Savage A., Browne I. W., Bolton J. G., 1976, MNRAS, 177, 77
Schaye J. et al., 2015, MNRAS, 446, 521
Schroetter I. et al., 2016, ApJ, 833, 39
Shen S., Madau P., Guedes J., Mayer L., Prochaska J. X., Wadsley J., 2013, ApJ, 765, 89
Shull J. M., Danforth C. W., Tilton E. M., Moloney J., Stevans M. L., 2017, ApJ, 849, 106
Somerville R. S., Davé R., 2015, ARA&A, 53, 51

Downloaded from https://academic.oup.com/mnras/article/497/1/498/5859973 by CNRS - ISTO user on 09 August 2022

Songaila A., Cowie L. L., 2010, ApJ, 721, 1448
Steidel C. C., Kollmeier J. A., Shapley A. E., Churchill C. W., Dickinson M., Pettini M., 2002, ApJ, 570, 526
Steidel C. C., Erb D. K., Shapley A. E., Pettini M., Reddy N., Bogosavljević M., Rudie G. C., Rakic O., 2010, ApJ, 717, 289
Stern J., Faucher-Giguere C.-A., Henawi J. F., Hafen Z., Johnson S. D., Fielding D., 2018, ApJ, 865, 91
Thom C., Chen H.-W., 2008, ApJS, 179, 37
Thom C. et al., 2012, ApJ, 758, L41
Tripp T. M., Sembach K. R., Bowen D. V., Savage B. D., Jenkins E. B., Lehner N., Richter P., 2008, ApJS, 177, 39
Tumlinson J., Peeples M. S., Werk J. K., 2017, ARA&A, 55, 389
Turner M. L., Schaye J., Steidel C. C., Rudie G. C., Strom A. L., 2014, MNRAS, 445, 794
Tytler D., 1982, Nature, 298, 427
van de Voort F., Schaye J., Altay G., Theuns T., 2012, MNRAS, 421, 2809
Vogelsberger M. et al., 2014, Nature, 509, 177
Wang L., Dutton A. A., Stinson G. S., Maccò A. V., Penzo C., Kang X., Keller B. W., Wadsley J., 2015, MNRAS, 454, 83
Weilbacher P. M., Streicher O., Urrutia T., Pécontal-Rousset A., Jarno A. R., 2014, in Manset N., Forshay P., eds, ASP Conf. Ser. Vol. 485, Astronomical Data Analysis Software and Systems XXIII. Astron. Soc. Pac., San Francisco, p. 451
Werk J. K., Prochaska J. X., Thom C., Tumlinson J., Tripp T. M., O'Meara J. M., Meiring J. D., 2012, ApJS, 198, 3
Werk J. K. et al., 2014, ApJ, 792, 8
Wijers N. A., Schaye J., Oppenheimer B. D., 2020, MNRAS , preprint (arXiv: 2004.05171)
Wild V. et al., 2008, MNRAS, 388, 227
Wisotzki L., Christlieb N., Bade N., Beckmann V., Köhler T., Vanelle C., Reimers D., 2000, A&A, 358, 77
Wotta C. B., Lehner N., Howk J. Christopher O., John M., Prochaska J. X., 2016, ApJ, 831, 95
Yin S. Y., Liang Y. C., Hammer F., Brinchmann J., Zhang B., Deng L. C., Flores H., 2007, A&A, 462, 535
York D. G. et al., 2000, AJ, 120, 1579
Zahedy F. S., Chen H.-W., Rauch M., Wilson M. L., Zabludoff A., 2016, MNRAS, 458, 2423
Zahedy F. S., Chen H.-W., Gauthier J.-R., Rauch M., 2017, MNRAS, 466, 1071
Zahedy F. S., Chen H.-W., Johnson S. D., Pierce R. M., Rauch M., Huang Y.-H., Weiner B. J., Gauthier J.-R., 2019, MNRAS, 484, 2257

APPENDIX A: GALAXY PROPERTIES IN THE MASSIVE GROUP AT $d_{\rm group} = 177$ PKPC FROM THE LLS AT $z_{\rm abs} = 0.6226$ TOWARDS J2135−5316

Optical spectra of the members of the LLS-associated galaxy group reported in Section 4.2.2 clearly show a wide range in the star formation histories among the members of the galaxy group, from young star-forming to old and evolved (Fig. 6). At $z = 0.6$, MUSE does not provide the spectral coverage necessary for observing Hα or [N II]. While the spectra cover higher order Balmer transitions and other nebular lines, only [O II] emission is consistently seen among all 10 group galaxies with the Ca II H&K absorption doublet and *G*-band absorption being the predominant features in five group members. In particular, the most luminous member of the group at $d = 244$ pkpc and $d\,v_{\rm gal} = -499$ km s^{-1} also displays a strong Balmer absorption series in addition to Ca II absorption (panel *i* in Fig. 6), characteristic of a post-starburst phase (see French et al. 2015; Rowlands et al. 2015 for recent references). It also shows [Ne III] and an [O III]/Hβ line ratio that suggests the presence of an active galactic nucleus (AGN).

Because of a lack of robust constraints for the dust content, we estimate an unobscured SFR based on the integrated [O II] line flux for each galaxy under the assumption that the presence of the [O II] lines is driven by the radiation field from young stars. To determine an integrated [O II] line flux and the velocity offset of each pixel, we employ a custom IDL code KUBEVIZ, kindly shared with us by M. Fossati, to fit the emission doublet (see Fossati et al. 2016 for a detailed description of the code). We first smooth the data cube using a 3 × 3 box in the image plane (corresponding to the size of the PSF) to improve the S/N per pixel without degrading the spatial resolution of the data. Then for the spectrum from each pixel, we fit the [O II] doublet using a double Gaussian function. KUBEVIZ takes into account the associated error for each spaxel in the fitting routine in order to suppress contributions from features due to sky subtraction residuals, and delivers the best-fitting integrated line flux and associated error of the doublet, along with the best-fitting velocity and velocity dispersion maps. We visually inspect the fitting results across the full field and repeat the fitting procedure as needed after modifying the input parameters. The total integrated [O II] line fluxes of the group galaxies range from $f_{\rm [OII]} = (5 \pm 1) \times 10^{-19}$ erg s^{-1} cm^{-2} to $f_{\rm [OII]} = (1.52 \pm 0.07) \times 10^{-16}$ erg s^{-1} cm^{-2}, leading to an unobscured SFR of ≈0.01–1.6 M$_\odot$ yr^{-1} based on the star formation calibrator of Kewley et al. (2004). The line-of-sight velocity map of the galaxy group is presented in the right-hand panel of Fig. 5.

An interesting feature of the spectra displayed in Fig. 5 is the contrast between ordinary continuum morphologies of the group galaxies in the pseudo *r*-band image and the irregular morphology of [O II] line emission around two massive group members at $dv_{\rm gal} = -129$ and -499 km s^{-1} to the south-west of the LLS. The extended [O II] emission morphologies of the two galaxies separated by ≈20 pkpc in projected distance and the large line-of-sight velocity spread from $dv \approx -500$ km s^{-1} to $dv \approx +100$ km s^{-1} imply that violent interactions may be taking place between the two galaxies, which may also be responsible for triggering the recent episode of star formation and possible AGN phase in the post-starburst galaxy at $dv_{\rm gal} = -499$ km s^{-1} and $d = 244$ pkpc (see e.g. Johnson et al. 2018).

APPENDIX B: LOW-MASS DWARFS AT $d \approx 26$ PKPC FROM THE LLS AT $z_{\rm ABS} = 0.3640$ TOWARDS J0248−4048

The three low-mass galaxies found in the vicinity of this LLS exhibit prominent nebular emission lines that are typical of star-forming regions (see Section 4.4.2 and Fig. 9). To systematically search for emission features associated with the LLS and to determine the velocity offsets, we use the KUBEVIZ software to fit line-emitting features at the redshift of the LLS in the full field covered by MUSE. We first smooth the data cube using a 3 × 3 box in the image plane. Then for the spectrum from each pixel, we fit all available strong emission lines (in this case, the [O II] doublet, Hβ, [O III] λλ 4960, 5008, and Hα; see Fig. 9 and next paragraph) simultaneously using a Gaussian function per line and adopting a common systemic redshift and velocity width across all lines considered. KUBEVIZ outputs the best-fitting integrated line flux and associated error for each line, along with the best-fitting velocity and velocity dispersion maps. Finally, we visually inspect the fitting results across the full field and repeat the fitting procedure as needed after modifying the input parameters. The line-of-sight velocity map of the three LLS-associated galaxies is presented in the right-hand panel of Fig. 8. No extended line emission is detected much beyond the optical extent of the three galaxies.

The presence of prominent nebular lines in all three galaxies enable a detailed analysis of the physical properties of these LLS-associated galaxies, including the SFR, ionization condition, ISM gas-phase metallicity, and dust content. We first estimate an unob-

Downloaded from https://academic.oup.com/mnras/article/497/1/498/5859973 by CNRS - ISTO user on 09 August 2022

scured SFR based on the total integrated Hα line flux ($f_{\rm H\alpha}$) in the MUSE data using the conversion from Kennicutt & Evans (2012), SFR $= 5.37 \times 10^{-42}\, L_{\rm H\alpha}\, {\rm M}_\odot\, {\rm yr}^{-1}$, which is based on a Chabrier (2003) stellar initial mass function. The galaxies have $f_{\rm H\alpha}$ ranging from $(6.3 \pm 0.2) \times 10^{-18}$ to $(4.41 \pm 0.03) \times 10^{-17}\, {\rm erg\, s^{-1}\, cm^{-2}}$, leading to an estimated SFR ranging from to 0.01 to 0.11 ${\rm M}_\odot\, {\rm yr}^{-1}$ (see columns 9 and 10 of Table 7).

Next, we examine the ionization condition of the gas by comparing the strong line ratios, [O III]/Hβ versus [N II]/Hα. None of the three galaxies exhibit a significant [N II] line, placing a 2σ upper limit on the $N2$ index, $N2 \equiv \log$ [N II] λ 6585/Hα, of $N2 < -1$. In addition, the [O III]/Hβ ratio of these galaxies ranges between $\log$ [O III]/H$\beta = 0.48$ and 0.52. Together, the observed [O III]/Hβ and [N II]/Hα ratios indicate that the ISM is ionized predominantly by young stars (e.g. Baldwin, Phillips & Terlevich 1981), rather than by active galactic nuclei (AGNs).

Finally, we estimate the ISM gas-phase metallicity and dust content using common emission-line calibrators. We first infer a 2σ upper limit to the ISM gas-phase metallicity of $12 + \log({\rm O/H}) < 8.3$ based on the absence of [N II] and the $N2$ calibration of Marino et al. (20132013), $12 + \log({\rm O/H}) = 8.74 + 0.46 \times N2$. Then we compute the R_{23} index, defined as $R_{23} \equiv$ ([O II] $\lambda\lambda$ 3726, 3729 + [O III] $\lambda\lambda$ 4960, 5008)/Hβ. For an accurate estimate of R_{23}, we assess the amount of dust extinction correction using the observed Hα/Hβ flux ratio. Following the prescription described in Calzetti et al. (2000),[4] we estimate the colour excess $E(B-V)$ according to $E(B-V) = 1.97 \log([f_{\rm H\alpha}/f_{\rm H\beta}]/2.86)$, and find $E(B-V) = 0.15 \pm 0.01$, 0.23 ± 0.04, and 0.07 ± 0.02 for the galaxies at $d = 15$, 37, and 150 pkpc, respectively. The wavelength-dependent extinction magnitude $A(\lambda)$ is related to $E(B-V)$ following $A(\lambda) = k(\lambda)E(B-V)$, where $k(\lambda)$ is the dust extinction law. Adopting the Calzetti (1997) extinction law, $k([{\rm O\,II}]) = 5.86$, $k({\rm H}\beta) = 4.60$, $k([{\rm O\,III}]) = 4.46$, and $k({\rm H}\alpha) = 3.33$. This exercise enables us to estimate the oxygen abundance using the R_{23} index based on extinction-corrected line ratios. Based on the calibration of Yin et al. (2007), $12 + \log({\rm O/H}) = 6.486 + 1.401 \times \log R_{23}$, which is justified by the upper limit of the $N2$ index, we find $12 + \log({\rm O/H}) = 7.7$, 7.5, and 7.6[5] for the galaxies with increasing d (see column 11 of Table 7). Uncertainties in the gas-phase metallicity are driven by the systematic uncertainty of the R_{23} calibration and it is estimated to be 0.1 dex (Yin et al. 2007).

While robust emission-line fluxes have been obtained for all three dwarf galaxies, accurate broad-band photometry is only feasible for the two galaxies at $d = 37$ and 150 pkpc, not affected by the glare of the QSO. The observed r-band magnitudes of these two galaxies are $AB(r) = 25.1$ and 24.1, respectively. We estimate an intrinsic r-band absolute magnitude M_r using a star-forming galaxy template and find $M_r = -16.3$ and -17.3 for the two galaxies, corresponding to 0.01 and 0.025 L_* adopting $M_{r_*} = -21.3$ for blue galaxies from Cool et al. (2012). We further estimate the underlying stellar mass $M_{\rm star}$ using the prescription for blue galaxies presented in Johnson et al. (2015), and find $\log M_{\rm star}/{\rm M}_\odot = 7.8$ and 8.2, respectively. Both galaxies are found to be exceedingly faint and low-mass. Based on the estimated ISM gas-phase metallicity of ≈10 per cent solar and adopting the mass–metallicity relation of dwarf galaxies (e.g. Berg et al. 2012), we argue that the closest galaxy at $d = 15$ pkpc is also likely to be a low-mass dwarf of $\log M_{\rm star}/{\rm M}_\odot \approx 8$. The observed and derived properties of these three galaxies are summarized in columns (2) through (11) of Table 7.

[4]Adopting the extinction law for the Small Magellanic Cloud from Gordon et al. (2003) does not change the extinction-corrected line ratios significantly.
[5]For comparison, the Sun has $12 + \log({\rm O/H})_\odot = 8.69 \pm 0.05$ (Asplund et al. 2009).

APPENDIX C: PROPERTIES OF A ROTATING DISC GALAXY AT $d = 67$ PKPC FROM THE LLS AT $z_{\rm ABS} = 0.4353$ TOWARDS J0357−4812

The optical spectrum of the absorbing galaxy is characterized by strong absorption features, together with weak [O II] and Hβ emission lines, indicating that this is an early-type galaxy (see Section 4.5.2 and Fig. 11). At $z = 0.4353$, MUSE does not provide the spectral coverage necessary for observing Hα, limiting our ability in obtaining robust constraints for the dust content, and consequently for the ISM gas-phase metallicity and ionization condition of the galaxy. However, the presence of the [O II] emission doublet does enable measurements of the velocity field across the galaxy as well as an estimate of the unobscured SFR. To determine an integrated [O II] line flux and the velocity centroid at each pixel, we fit the emission doublet using KUBEVIZ, visually inspect the fitting results across the full field, and repeat the fitting procedure as needed after modifying the input parameters. We find a total integrated [O II] line flux over the entire galaxy of $f_{\rm [OII]} = (6.14 \pm 0.06) \times 10^{-17}\, {\rm erg\, s^{-1}\, cm^{-2}}$, leading to an unobscured SFR of $\approx 0.28\, {\rm M}_\odot\, {\rm yr}^{-1}$ based on the star formation calibrator of Kewley et al. (2004).

The observed velocity gradient along the long axis in panel (b) of Fig. 10 supports the presence of a rotating disc. To investigate the relative motion of the LLS with respect to the rotation of the galaxy, we first estimate the inclination and orientation of the underlying disc using the pseudo r-band image. The outline of the galaxy appears to be largely well defined by an ellipse in the pseudo r-band image with a mild irregular feature towards the north-west corner, as suggested also by the [O II] emitting morphology. We find that the galaxy can be characterized by an inclination angle of $i \approx 44^\circ$ and a position angle of the major axis of $\alpha \approx 120^\circ$, north through east. If there exists an extended gaseous disc, then the QSO sightline probes the gas at $\approx 27^\circ$ from the major axis. Next, we de-project both the projected distance d and ${\rm d}v_{\rm gal}$ observed along the major axis on to the disc plane. Following the prescription described in Chen et al. (2005), the galactocentric radius R is related to d according to $R = d\sqrt{1 + \sin^2(\phi - \alpha)\tan^2(i)}$, while the de-projected velocity is related to the observed line-of-sight velocity according to $\Delta\, v_{\rm deproj} = \Delta\, v\sqrt{1 + \sin^2(\phi - \alpha)\tan^2(i)}/\cos(\phi - \alpha)/\sin(i)$, where ϕ is the position angle of the slit. For the galaxy disc, the MUSE data cube enables us to place a pseudo slit along the major axis, in which case $\phi_{\rm gal} = \alpha$, whereas for the LLS ϕ is dictated by the location of the QSO probe relative to the galaxy and we find $\phi_{\rm QSO} \approx 93^\circ$.

The de-projected rotation velocity along the disc plane as a function of galactocentric radius in panel (c) of Fig. 10 also includes the three strongest H I absorbing components (c1, c2, and c3 from Table 6) of the LLS along the QSO sightline for comparison (open circles in panel c of Fig. 10). Under the assumption that the gas is moving along the plane extended from the inclined optical disc, the zero velocity in panel (c) of Fig. 10 corresponds to the systemic redshift of the galaxy. While the rotation curve appears to flatten at ${\rm d}v_{\rm deproj} \approx +225$ km s^{-1} on the east side of the galaxy, it continues to extend beyond $|{\rm d}v_{\rm deproj}| \approx 300$ km s^{-1} on the west side which is likely related to the extended structure revealed in [O II] emission.

This paper has been typeset from a TEX/LATEX file prepared by the author.

Downloaded from https://academic.oup.com/mnras/article/497/1/498/5859973 by CNRS - ISTO user on 09 August 2022